Plastic deformation of tubular crystals by dislocation glide

Daniel A. Beller[1] and David R. Nelson[2]
[1]*John A. Paulson School of Engineering and Applied Sciences, Harvard University, Cambridge, Massachusetts 02138, USA*
[2]*Department of Physics, Harvard University, Cambridge, Massachusetts 02138, USA*
(Received 1 May 2016; revised manuscript received 31 August 2016; published 26 September 2016)

Tubular crystals, two-dimensional lattices wrapped into cylindrical topologies, arise in many contexts, including botany and biofilaments, and in physical systems such as carbon nanotubes. The geometrical principles of botanical phyllotaxis, describing the spiral packings on cylinders commonly found in nature, have found application in all these systems. Several recent studies have examined defects in tubular crystals associated with crystalline packings that must accommodate a fixed tube radius. Here we study the mechanics of tubular crystals with variable tube radius, with dislocations interposed between regions of different phyllotactic packings. Unbinding and separation of dislocation pairs with equal and opposite Burgers vectors allow the growth of one phyllotactic domain at the expense of another. In particular, glide separation of dislocations offers a low-energy mode for plastic deformations of solid tubes in response to external stresses, reconfiguring the lattice step by step. Through theory and simulation, we examine how the tube's radius and helicity affects, and is in turn altered by, the mechanics of dislocation glide. We also discuss how a sufficiently strong bending rigidity can alter or arrest the deformations of tubes with small radii.

DOI: 10.1103/PhysRevE.94.033004

I. INTRODUCTION

In botany, the arrangements of leaves around a stem, seeds on a pine cone, spines on a cactus, scales on a pineapple, etc., often follow beautifully regular spiraling patterns—a subject of interest for centuries—known as phyllotaxis ("leaf arrangement") [1–4]. The spirals of nearest-neighbor connections, known as parastichies, form families of parallel curves characterized by integer indices called parastichy numbers, indicating the number of distinct spirals in the family [see Figs. 1(a) and Fig. 2(b)]. An intriguing feature of botanical phyllotaxis is the widespread appearance of parastichy numbers that are successive members of the Fibonacci sequence (or of similar sequences called the double Fibonacci sequence and the Lucas sequence [3,4]). In Fibonacci phyllotaxis, the divergence angle d, the azimuthal angle between consecutive sites (ordered by radius or height), is then approximately related to the golden mean $\varphi = \frac{1}{2}(1+\sqrt{5})$ by $d \approx 2\pi(1-\varphi^{-1}) \approx 137.5^\circ$ [1–4].

In recent decades, there has been a growing appreciation of the importance of phyllotaxis outside of botany; it can also arise in physical systems under the general scenario of isotropically repulsive particles self-organizing on a compressing cylinder or a growing disk. Levitov predicted that repulsive vortices in a type II superconductor would naturally converge toward Fibonacci parastichy numbers [5,6]. Fibonacci spirals were soon thereafter observed in experiments on repulsive ferrofluid drops in a magnetic field [7]. Recently, the dynamics of such phyllotactic growth has been studied in a "magnetic-cactus" model of repulsive magnets on a cylinder [8,9].

More generally, regular helical packings on cylinders that do not necessarily follow the Fibonacci or Lucas sequences are widespread in biology and physics. Such systems were called "tubular crystals" by Erickson [10], who suggested that the geometrical language of phyllotaxis, including the parastichy number labeling, is a natural description for such systems. He had in mind tubular assemblies in microbiology such as rodlike viruses or bacteriophage tails, bacterial flagella, and intracellular biofilaments such as actin and microtubules. Packings of spherical particles in cylindrical capillaries or on cylindrical surfaces also show more general phyllotactic arrangements [11–13]. Covalently bonded single-walled carbon nanotubes (SWCNTs) and related materials such as boron nitride nanotubes provide further important examples: Their hexagonal unit cells form helical lattice lines along the tube, with a traditional labeling by a pair of integer indices in correspondence with the parastichy numbers of phyllotaxis [14]. It is interesting to note that connections between phyllotaxis and crystallography on a periodic space date back to foundational work in botanical phyllotaxis by the botanist Louis Bravais and his brother, crystallographer Auguste Bravais [15].

In this paper, we study the mechanics of plastic deformation of tubular crystals via the nucleation and glide separation of pairs of dislocation defects in the tubular lattice. The motion of these dislocations causes a *parastichy transition*, i.e., a change in the parastichy numbers of the tubular crystal [16], thus providing a low-energy mode for the release of externally imposed strain. For maximum simplicity, we focus on triangular lattices, which are described by an isotropic elastic tensor, and treat the tubes as thin-sheet materials. In simulations, we model these materials as networks of harmonic springs with a bending rigidity. In the continuum limit, the elastic interactions of dislocations on perfectly cylindrical surfaces of fixed radius have recently been studied [17]. Here we focus on the changes in tube radius and helicity that accompany the parastichy transitions for a finite-sized elastic network subject to plastic deformations.

We calculate the critical stresses required to plastically deform tubular crystals by dislocation pair nucleation and glide motion. From among several possible dislocation-pair orientations, we identify the pairs that unbind at lowest applied stress. As each defect orientation possibility represents a different parastichy transition, we identify pathways of plastic deformation through the space of parastichy numbers under successive dislocation pair unbindings, both analytically and through numerical modeling. These pathways reveal stable

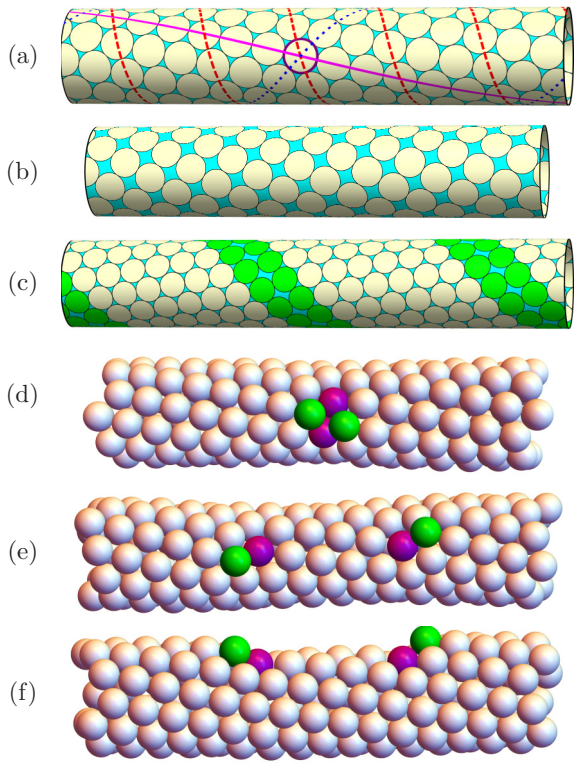

FIG. 1. (a) A triangular lattice of disks in a cylindrical surface. The three parastichies intersecting at the disk outlined in the purple (dark gray) ring are shown as the magenta (solid), blue (dotted), and red (dashed) helices. (b) A rhombic packing of disks in a cylindrical surface. (c) A triangular packing of disks in a cylindrical surface with a spiral line-slip defect or "stacking fault." The disks in contact with the line-slip defect have reduced coordination number (five neighbors instead of six) and are colored green (gray). (d) A tubular crystal consisting of a triangular packing of spheres interrupted by the nucleation of a dislocation pair, producing two five-coordinated spheres labeled green (medium gray) and two seven-coordinated spheres labeled magenta (dark gray). (e) The dislocations nucleated in (d) are now spatially separated. (f) A different view of the tubular crystal in (e), highlighting that the region between the dislocations is narrower than the region outside the dislocations.

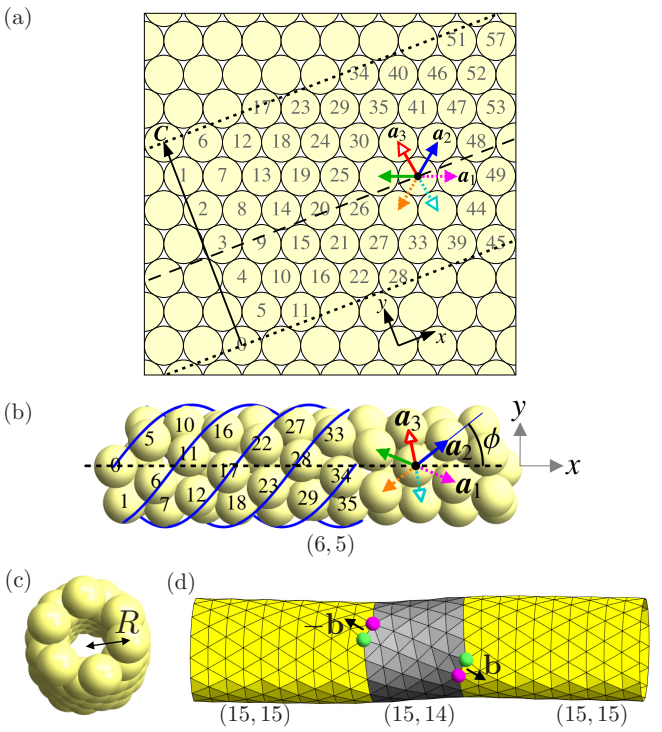

FIG. 2. Schematic illustration of the phyllotactic arrangement of sites in tubular triangular crystals. (a) 2D triangular packing of disks, with a circumference vector **C** selected to roll the planar lattice into a cylinder with phyllotactic indices $(m,n) = (6,5)$ by identifying the two dotted lines, giving a cylinder axis parallel to the dashed line. The six primitive lattice directions are shown as the six colored arrows. Number labels are the axial index of the lattice sites in order of increasing x coordinate. (b),(c) The tubular crystal with $(m,n) = (6,5)$, a triangular packing of spheres approximating the cylindrical packing of disks obtained from (a), in both side (b) and top (c) views. The geometrical parameters ϕ, describing the lattice orientation, and R, the tube radius, are shown in (b) and (c), respectively. Blue helices in (b) follow portions of the five parastichies along $\mathbf{a}_2$. The $\mathbf{a}_i$ arrow legend in (a) and (b) identifies lattice directions in the planar crystal with the lattice directions in the tubular crystal's tangent plane. (d) Plastic deformation of a tubular crystal from an initial $(m,n) = (15,15)$ configuration in yellow (light gray) to an $(m',n') = (15,14)$ configuration in dark gray by glide of a dislocation pair with $\mathbf{b} = \mathbf{a}_1$; the figure shows a snapshot of the deformation process as the dislocations glide apart. Positive and negative disclinations are marked by green (medium gray) and magenta (dark gray) spheres, respectively.

and unstable crystal lattice orientations under axial or torsional applied stress.

We show that a bending rigidity helps to stabilize tubular crystals against axial elongation, and we identify a regime in which the bending rigidity destabilizes narrow tubes with respect to spontaneous tube-widening deformations. These effects of the bending energy in simulation are well-described by continuum theory predictions. Additionally, during the plastic deformation process we find that the dislocations cause reorientations of the tube axis, as well as nontrivial tube radius profiles in the transition regions between different phyllotactic tessellations. We provide analytical descriptions of both geometrical effects.

When disks are packed on a cylindrical surface of *fixed* radius R, incommensurability of a perfect triangular lattice with the azimuthal periodicity $2\pi R$ can cause the ground state either to distort into a strained rhombic lattice, such as the one depicted in Fig. 1(b) [16,18], or else to develop a one-dimensional, helical "line-slip" defect interrupting an otherwise triangular packing like the one in Fig. 1(c) [19]. The same is true for packings of spheres that are constrained to lie in contact with a solid cylinder, as the sphere centers all sit at a fixed radius R from the center line [13,20,21]. The relative stability of uniform rhombic packings versus line-slip packings has been shown recently to depend on the softness of the interparticle potential [13].

Our focus here is on a different kind of system: Although we retain the tube topology, we remove the constraint of a perfectly cylindrical substrate or wall of fixed radius, instead allowing the tubular crystal's shape to vary as a function of

space and time. The tube shape is determined by the energy-minimizing positions of sites with a given bond network, possibly including defects. By construction, in this system there are no line-slip defects or extended rhombic packings. Instead, the triangular lattice tessellation is interrupted only by isolated dislocations nucleating in pairs, as depicted in Fig. 1(d), and moving by successive bond flips (see Fig. 4) to produce intermediate states like the one shown in Figs. 1(e) and 1(f). The total number of bonds in the lattice is conserved in this process. The tube radius and the orientation of the lattice on the tube both adjust in response to the passage of a dislocation through the system, due to well-established geometrical rules that we describe in Sec. II. For example, the tubular crystal in Figs. 1(e) and 1(f) is narrower in the region between the dislocations than in the region outside. Further motion of the dislocations away from each other expands the new, narrower tessellation at the expense of the original, wider one, resulting in a plastically deformed tubular crystal.

These considerations describe SWCNTs, where the honeycomb lattice of hexagons can be interrupted by dislocations composed of pentagon-heptagon pairs. Such dislocations can arise and move through the lattice via successive carbon-carbon bond rotations, called Stone-Wales rotations, altering the tube's radius and helicity in the process [22]. Detailed quantum mechanical simulations have been employed to study plastic deformation of these objects by dislocation motion [23–27], and there is experimental evidence confirming the role of defect motion in the plasticity of strained nanotubes [28–30]. One reason for the importance of such dislocation-mediated deformations is that the resulting change in phyllotactic indices alters the SWCNT's electronic properties [22,25]. In addition, the presence of dislocations within a SWCNT provides a source of disorder that decreases the conductivity [29,31].

Microtubules offer another example of helical tubular crystals, in this case composed of tubulin proteins, where the tube radius is determined by the crystalline network. Microtubules are biofilaments responsible for the mechanics of the eukaryotic cytoskeleton and are especially important in cell division [32]. Here dimers of the protein tubulin assemble into protofilaments parallel or nearly parallel to the tube axis, with an axial shift between adjacent protofilaments giving rise to the shallower helical parastichy [33]. Microtubules have been observed to change protofilament number along their length, strongly suggesting the presence of dislocations [34].

Dislocation-mediated plastic deformation has also been suggested as a mechanism for the growth of rod-shaped bacteria such as *E. coli*, via circumferential climb motion of dislocations in the peptidoglycan network of the bacterial cell wall, with new material added to the wall at each climb step [35–37]. Plastic bending deformations of growing bacteria can also be understood in the context of this model [38].

Dislocations are, furthermore, readily apparent in botanical phyllotaxis, where parastichies begin or end in association with a parastichy transition as the radius changes. In many cases, such as the prototypical example of the sunflower head, dislocations are arranged in ring-shaped grain boundaries to accommodate the advancement of the parastichy numbers through the Fibonacci or Lucas series, in so-called *rising phyllotaxis* [3,39,40]. On the other hand, some plants regularly possess isolated dislocations allowing parastichy number shifts of ± 1 as the radius changes, akin to our focus in this paper. Examples of such plants include many cacti, the firmoss *Lycopodium selago*, and scales on the fruit of the Raffia palm [3,39].

The rest of this paper is organized as follows. In Sec. II we describe the phyllotactic geometry of tubular crystals and the parastichy transformations caused by the unbinding of dislocations. Section III gives the predictions of continuum elasticity for the mechanics of plastic deformation in tubular crystals, first without a bending energy and then with a bending energy introduced as an important perturbative correction. Section IV presents results of numerical simulations modeling tubular crystals as networks of harmonic springs with a bending energy, probing the critical axial tension required to unbind and separate dislocation pairs over a wide range of tube geometries. We also investigate reorientation of the tube axis caused by the presence of dislocations. Finally, in Sec. V we examine the change in radius of the tube within the *transition region* around an isolated dislocation, including an interesting oscillatory behavior of the radius profile.

II. PHYLLOTACTIC DESCRIPTION OF TUBULAR CRYSTALS

A. Pristine tubular crystals

In the study of phyllotaxis, the helical arrangements of leaves, petals, etc., are described in terms of the helices along directions of nearest-neighbor contacts, called *parastichies* [41]. These contacts define lattice directions of an associated 2D lattice that has been rolled into a cylinder. Each parastichy is a member of a family of stacked parastichy helices, related by translations along the cylinder axis. Figure 1(a) shows three parastichies threading through a particular lattice site in a triangular lattice, while the blue (dark gray) helices in Fig. 2(b) comprise the parastichy family consisting of all parastichies along the direction $\pm\mathbf{a}_2$ as labeled in the figure. Each parastichy family collectively accounts for all lattice sites. The number of distinct members of a particular parastichy family gives a *parastichy number*. If all the lattice sites are ordered by their height along the cylinder's axis and labeled with an *axial index* i, then two sites neighboring along a parastichy of parastichy number q will differ in their axial indices by $\Delta i = q$ [3,15,41].

For a triangular lattice, there are three families of parastichies, and the tubular crystal tessellation is described by a triple of integer parastichy numbers $(|n-m|,n,m)$. If all three (positive) parastichy numbers have a common factor $k > 1$, then the lattice has a k-fold rotational symmetry, where k is known as the *jugacy*. Since the first of the three parastichy numbers is the difference of the other two, a triangular lattice tessellation of a tubular crystal can be uniquely labeled by an ordered pair of parastichy numbers. We choose to use the representation (m,n), where m is the parastichy number of the steepest right-handed helix, and n that of the steepest left-handed helix. The indices are then restricted to the range $\frac{1}{2}n \leqslant m < 2n$.

The geometry of a pristine tubular packing of spheres or the hexagons of a carbon nanotube is well approximated by a triangular packing of disks in the surface of a cylinder [10,16],

and the latter situation is much easier to describe with precision. Consider a triangular packing of disks in the plane, with two primitive lattice vectors $\mathbf{a}_1$ and $\mathbf{a}_2$, where $\mathbf{a}_2$ is oriented 60° counterclockwise from $\mathbf{a}_1$ and both vectors have length equal to the lattice spacing a. As shown in Fig. 2, we can roll up the packing into a tube by choosing a lattice vector $\mathbf{C} = c_1\mathbf{a}_1 + c_2\mathbf{a}_2$, with $c_1, c_2 \in \mathbb{Z}$, to serve as a circumference vector (also referred to as the characteristic vector), so that lattice sites separated by $\mathbf{C}$ in the plane are mapped to the same site on the cylinder. Since every step upward along the n parastichy raises the axial index by $\Delta i = n$, and likewise every step downward along the m parastichy lowers the axial index by $\Delta i = -m$, the circumference vector can be expressed as $\mathbf{C} = -n\mathbf{a}_1 + m\mathbf{a}_2$. The resultant path has a net change of $\Delta i = -nm + mn = 0$ in the axial index, as must be true for a path beginning and ending at the same point on the cylinder. The radius of the tube [Fig. 2(c)] is therefore, to an excellent approximation in all but the smallest-diameter tubes,

$$R \approx \frac{1}{2\pi}|\mathbf{C}| = \frac{a}{2\pi}\sqrt{m^2 + n^2 - mn}. \tag{1}$$

The orientation of the lattice on the tube can be described by the angle ϕ that the n parastichy, the steepest left-handed helix of nearest neighbors, makes with the cylinder axis:

$$\tan\phi \approx \frac{2}{\sqrt{3}}\left(\frac{m}{n} - \frac{1}{2}\right). \tag{2}$$

Using the n parastichy to define ϕ is, of course, arbitrary; in general, the lattice directions make angles $\phi + q\pi/3$, $q \in \mathbb{Z}$, with the cylinder axis. For a pristine (defect-free) tubular crystal in mechanical equilibrium, the pair of "geometrical descriptors" (R,ϕ) is thus in one-to-one correspondence with the pair of parastichy numbers (m,n) that identifies the tessellation of the tubular crystal. Our choice $\frac{1}{2}n \leqslant m < 2n$ restricts ϕ to the interval $0 \leqslant \phi < 60°$. Figures 2(a) and 2(b) introduce a color code for the six primitive lattice directions that we use throughout this paper. Equations (1) and (2) are exact for a packing of disks in a cylindrical surface and nearly exact for all but the few smallest tubular crystals; more complicated, implicit equations for the geometrical parameters of a tubular crystal may be solved numerically to give R and ϕ exactly [10,16].

Two ϕ values correspond to achiral packings. For $\phi = 0$, we have $m = \frac{1}{2}n$ and one of the parastichies is a straight line along the cylinder axis. The "armchair" single-walled carbon nanotube geometry has its hexagons centered on such a lattice [14]. The other achiral configuration has $\phi = 30°$, $m = n$, and one of the parastichies is a circle around the cylinder's circumference; this corresponds to the hexagon centers in the "zigzag" nanotube geometry.

B. Geometry of plastic deformation

If a tubular crystal is to undergo plastic deformation changing R and ϕ, how can we accomplish the necessary *parastichy transition* altering (m,n)? One option, termed "continuous contraction" by Harris and Erickson [16], is to break contacts along one of the parastichies uniformly throughout the lattice, thus replacing the triangular packing with a rhombic one [see Fig. 1(b)], and to distort the rhombic packing until a new set of contacts is made, reestablishing the triangular lattice with a new pair of parastichy numbers [18]. Such continuous contractions are the basis for parastichy transitions in botany and are essential to understanding the widespread appearance of numbers from the Fibonacci and similar sequences as parastichy numbers [2,4]. Levitov studied continuous transitions for two-dimensional lattices of repulsive particles under compression, finding a physical basis for the prevalence of Fibonacci parastichy numbers in this scenario [5,6]. However, in a physical context, such transitions typically involve large energy barriers, proportional to the length of the parastichy with broken bonds.

Here we instead examine a much more localized (and lower energy) type of parastichy transition: the motion of a dislocation pair through the triangular lattice. Each dislocation can be viewed as a pair of point disclinations, a positive disclination at a five-coordinated site and a negative disclination at a seven-coordinated site (see, e.g., [42]). The dislocation is characterized by a Burgers vector $\mathbf{b} = -\oint(\partial\mathbf{u}/\partial l)dl$, where $\mathbf{u}$ is the vector field of displacements from the pristine lattice and the integration is along a counterclockwise Burgers circuit enclosing the dislocation [43]. From a pristine triangular lattice, a pair of dislocations with Burgers vectors $\mathbf{b}$, $-\mathbf{b}$ can be created by a bond flip, transforming four six-coordinated sites to a pair of 5-7 disclination pairs (see Fig. 4). Here $\mathbf{b}$ is a two-dimensional vector, $\mathbf{b} = b_1\mathbf{a}_1 + b_2\mathbf{a}_2$, with $b_1, b_2 \in \mathbb{Z}$.

The dislocations can then mediate plastic deformations by moving through the lattice by either glide (along the directions $\pm\mathbf{b}$) or climb (perpendicular to $\mathbf{b}$) via successive local rearrangements. As the pair of dislocations moves apart, a region of tubular crystal with a different circumference vector $\mathbf{C}' = \mathbf{C} + \mathbf{b}$, grows between the two dislocations, at the expense of the original tubular tessellation $\mathbf{C}$ [16]. Following the "Frank criterion" [44], we will consider only dislocations with Burgers vectors equal to the primitive lattice vectors, $\mathbf{b} = \pm\mathbf{a}_1$, $\pm\mathbf{a}_2$, or $\pm\mathbf{a}_3$, where $\mathbf{a}_3 = \mathbf{a}_2 - \mathbf{a}_1$. Therefore, each parastichy transition changes each of m,n by either ±1 or 0, as given in Table I.

For comparison, the high-energy barrier, continuous contraction process described above results in one of the (usually more drastic) parastichy transitions $(\Delta m,\Delta n) \in \{(-n,0),(0,m),\pm(m-n,m-n)\}$ if $m > n$, or $(\Delta m,\Delta n) \in \{(0,-m),(n,0),\pm(n-m,n-m)\}$ if $n < m$ [16]. (If $m = n$ then the only available continuous contraction doubles n.)

Figure 2(d) illustrates the plastic deformation of a tubular crystal with initial parastichy numbers $(m,n) = (15,15)$, the outer yellow (light gray) region, into a new tessellation $(m',n') = (15,14)$, the central dark gray region, by glide motion of a dislocation pair whose right-moving dislocation has $\mathbf{b} = \mathbf{a}_1$. The central dark gray region is slightly narrower than the outer yellow (light gray) region [as in Figs. 1(e) and 1(f)], and the purely circumferential parastichies in the

TABLE I. Allowed transitions of m and n.

b	$\mathbf{a}_1$	$\mathbf{a}_2$	$\mathbf{a}_3$	$-\mathbf{a}_1$	$-\mathbf{a}_2$	$-\mathbf{a}_3$
Δm	0	+1	+1	0	−1	−1
Δn	−1	0	+1	+1	0	−1

outer region become a single shallow helix in the central region. The lattice sites of the tubular crystal are here the nodes of a discretized surface, as simulated using the method described in Sec. IV.

We restrict our attention to dislocation glide and not climb. Glide is more relevant to colloidal cylindrical crystals, provided the density of vacancies and interstitials is low, and exit and entry of colloidal particles to and from the surrounding medium are rare events. Climb dynamics is more natural in the context of elongating bacteria, where the extra material needed for climb comes from metabolic processes inside the cell [36]. Because a dislocation can glide either parallel or antiparallel to its Burgers vector, we have a total of six distinct Burgers vector pairs $\pm\mathbf{b}$ to consider for each (m,n).

III. MECHANICS OF PLASTIC DEFORMATION: ANALYTIC PREDICTIONS

A. Critical stresses for dislocation pair unbinding with a stretching energy

Our goal is to understand the mechanics of plastic deformation in tubular crystals, as mediated by dislocation glide. We start with the usual elastic free energy of bond stretching and compression for isotropic two-dimensional, planar crystals,

$$F_s = \frac{1}{2}\int dA\left(2\mu u_{ij}u_{ij} + \lambda u_{kk}^2\right), \tag{3}$$

where the sixfold symmetry of a triangular lattice is sufficient to ensure isotropy [43]. Here μ and λ are the Lamé coefficients, and $u_{ij}(\mathbf{x}) = \frac{1}{2}[\partial_i u_j(\mathbf{x}) + \partial_j u_i(\mathbf{x})]$ is the strain tensor in terms of the displacement vector field $\mathbf{u}(\mathbf{x})$. The two-dimensional Young's modulus is $Y = 4\mu(\mu+\lambda)/(2\mu+\lambda)$ [45].

In a stress tensor field $\sigma_{ij}(\mathbf{x})$, a dislocation with Burgers vector $\mathbf{b}$ experiences a force

$$f_i = b_k\sigma_{jk}\epsilon_{ijz}, \tag{4}$$

known as the Peach-Koehler force [43,44], where ϵ_{ijz} is the Levi-Civita tensor. On an infinite plane (as opposed to a cylinder), the interaction energy of two dislocations with opposite Burgers vectors $\mathbf{b}$, $-\mathbf{b}$ gliding apart with separation $\mathbf{r} = r\mathbf{b}/|\mathbf{b}|$ is [44,46]

$$F_s(\mathbf{r}) = A|\mathbf{b}|^2\ln(r/a) - b_k\sigma_{jk}^{\rm ext}\epsilon_{ijz}r_i + 2E_c, \tag{5}$$

where $A \equiv Y/(4\pi)$, $\sigma_{jk}^{\rm ext}$ is a constant external stress tensor field, a is the lattice constant, and E_c is the core energy of a dislocation. Let θ be the angle between $\mathbf{b}$ and a preferred direction $\hat{\boldsymbol{x}}$ [this will ultimately become the cylinder axis; see Figs. 2(a) and 2(b)]. Under the Frank criterion $|\mathbf{b}| = a$, the elastic energy reduces to

$$F_s(r) = Aa^2\ln(r/a) + \frac{1}{2}\left(\sigma_{xx}^{\rm ext} - \sigma_{yy}^{\rm ext}\right)sar\sin(2\theta) - \sigma_{xy}^{\rm ext}sar\cos(2\theta) + \text{const.}, \tag{6}$$

where $s \equiv \text{sgn}[\mathbf{b}\cdot\hat{\boldsymbol{x}}]$, which is $+1$ (or -1) if the dislocations increase their separation by gliding parallel (or antiparallel) to their Burgers vectors. We take the Burgers vector $\mathbf{b}$ to belong to the dislocation gliding with projection along the $+\hat{\boldsymbol{x}}$ direction. The corresponding force along the glide direction is then

$$f_g(r) = -A\frac{a^2}{r} - \frac{1}{2}\left(\sigma_{xx}^{\rm ext} - \sigma_{yy}^{\rm ext}\right)sa\sin(2\theta) + \sigma_{xy}^{\rm ext}sa\cos(2\theta). \tag{7}$$

At small separation r, the force is dominated by the attractive stress field of the dislocation pair. At large r, however, the dislocations can be driven apart, depending on the signs of the components of $\sigma^{\rm ext}$ and the value of θ. In this case, the force vanishes at a maximum in the one-dimensional energy landscape [17,47], at separation

$$r^* = \frac{sAa}{\sigma_{xy}^{\rm ext}\cos(2\theta) - \frac{1}{2}\left(\sigma_{xx}^{\rm ext} - \sigma_{yy}^{\rm ext}\right)\sin(2\theta)}. \tag{8}$$

If we set r^* equal to the lattice constant a, we can find the critical stress values necessary to pull apart a dislocation pair nucleated from the pristine lattice by a single bond flip [see Fig. 1(d) or Fig. 4(b)]. These critical stresses, which we denote with a dagger symbol, are given by

$$(\sigma_{xx} - \sigma_{yy})^\dagger = -2sA/\sin(2\theta), \tag{9}$$

$$\sigma_{xy}^\dagger = sA/\cos(2\theta). \tag{10}$$

While continuum elasticity theory is expected to break down at the scale of the lattice constant a, we find in Sec. IV that continuum theory predictions obtained by setting $r^* = a$ nevertheless yield quantitative insights into numerically modeled tubular crystals.

On a cylinder, the energetics of a dislocation pair at finite glide separation is different than on the plane, as each dislocation feels the stress field of all the periodic images of the other dislocation, so the dislocation pair interacts like a pair of grain boundaries in the infinite plane. The dislocation pair energy on a cylinder was calculated in Ref. [17], and for a separation x along the cylinder axis and y along the azimuthal direction can be written (up to a constant for fixed θ) as

$$\frac{F_s(x,y)}{Aa^2/2} = \ln[\cosh\tilde{x} - \cos\tilde{y}] + \tilde{x}\left[\frac{\sinh\tilde{x}\cos(2\theta) + \sin\tilde{y}\sin(2\theta)}{\cos\tilde{y} - \cosh\tilde{x}}\right] + \frac{2R}{a}[\tilde{\sigma}_{xy}(\tilde{y}\sin\theta - \tilde{x}\cos\theta) - \tilde{\sigma}_{yy}\tilde{x}\sin\theta + \tilde{\sigma}_{xx}\tilde{y}\cos\theta], \tag{11}$$

where we use dimensionless quantities $\tilde{x} \equiv x/R$, $\tilde{y} \equiv y/R$, and $\tilde{\sigma}_{ij} = \sigma_{ij}^{\rm ext}/A$. Thus, at separations large compared to the cylinder radius R, the dislocations attract with a linear potential [second term of Eq. (11)] that can compete with the linear term from the external stress.

For dislocation separations small compared to the cylinder radius, $r \ll R$, the stretching energy for dislocations on a cylinder reduces to that on a plane. Therefore, in examining the stress required to unbind and separate a dislocation pair from an initial separation of one lattice spacing, it is appropriate to start with the stretching energy of Eq. (6), giving the critical stresses in Eqs. (9) and (10). Those critical stresses are of order $A = Y/(4\pi)$, whereas the stress magnitude required to

ensure that dislocations continue to glide apart at large distance $x \to \infty$ is of smaller order $\sim(a/R)A$, as obtained from the form of Eq. (11) [17]. Therefore, an imposed stress great enough to unbind a dislocation pair at separation $r = a$ is sufficient to ensure continued glide to infinite separation.

Our continuum approach to dislocation energetics neglects a small periodic Peierls potential arising from the discreteness of the underlying lattice, as well as the associated Peierls stress needed to overcome it [44]. In this paper, we assume a small nonzero temperature sufficient to allow easy passage over these corrections to our continuum energy formulas. Even without a small temperature to help overcome the Peierls barrier, the size of the critical stresses $\sigma^\dagger \sim A$ alone may be sufficient, as the maximum Peierls stress is typically several orders of magnitude smaller than $\mu \sim A$ [44].

The external stress typically acts to pull apart three of the six possible dislocation pairs with elementary, opposite Burgers vectors, whereas the other three dislocation pairs are pushed together. The critical stress values of Eqs. (9) and (10) do not depend on R, as the energetics at these tight separations are the same as on the plane; however, they do depend on the lattice orientation ϕ with respect to the cylinder axis through the parastichy angle $\theta = \phi + q \cdot 60^\circ$, $q \in \mathbb{Z}$. On the other hand, each dislocation unbinding event changes both R and ϕ. [Recall from Sec. II that we define ϕ as the angle made by the steepest left-handed parastichy with $\hat{\boldsymbol{x}}$, the cylinder axis; see Eq. (2).]

The critical stresses of Eqs. (9) and (10) for dislocation unbinding are plotted in Fig. 3 using the color scheme introduced in Fig. 2 for the Burgers vector $\mathbf{b}$. The arrows on the curves in Fig. 3 record whether ϕ increases or decreases as a result of the associated plastic deformation event. If a tubular crystal with a given parastichy tilt ϕ is subjected to an external stress that slowly rises from zero until a dislocation unbinding event occurs, then we need only examine the Burgers vector pair with the lowest critical stress $\sigma^\dagger$ at a given ϕ. In this scenario, for pure axial stress $\sigma^\dagger_{xx} > 0$, we see in Fig. 3(a) a "flow" in ϕ away from 0 or 60° and toward 30°, while the cylinder radius decreases. Because $\phi = 30^\circ$ is an achiral geometry, the tube will thus evolve toward an (approximately) achiral state as its radius shrinks. This deformation pathway is in qualitative agreement with molecular dynamics simulations of carbon nanotubes showing that in the ductile regime of $\sim 10\%$ strain and high temperature, plastic deformations rotate the graphene orientation on the tube away from the armchair state ($\phi = 0$) and toward the zigzag state ($\phi = 30^\circ$) [22,23].

For an applied stress $\sigma^\dagger_{xy}$ that is purely torsional, Fig. 3(b) reveals a flow away from $\phi = 45^\circ$ and toward $\phi = 15^\circ$. If the sign of σ^{ext}_{xy} is reversed, $\phi = 15^\circ$ becomes unstable and $\phi = 45^\circ$ becomes stable. Meanwhile, the radius changes nonmonotonically, depending on the value of ϕ. Interestingly, molecular dynamics simulations of SWCNTs under torsion [26] have found that $\phi = 15^\circ$ is a critical angle at which there is a change in Burgers vector of the dislocation pair that becomes stable relative to the pristine lattice at lowest torsional strain and at which the torsional strain per unit length γ^* required to unbind this dislocation pair has a cusp qualitatively similar to that in Fig. 3(b). Equation (10) therefore appears to offer geometric intuition for those numerical findings.

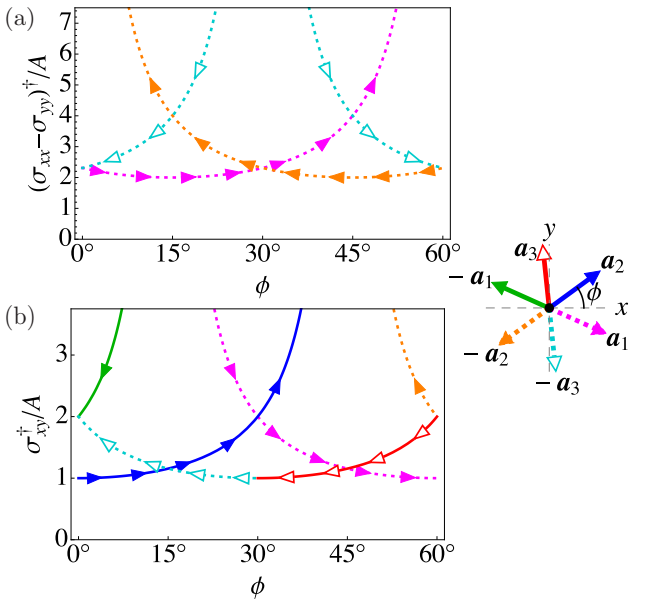

FIG. 3. Dimensionless critical external stress values required to unbind a dislocation pair with initial separation of one lattice spacing, for different lattice orientations ϕ, as given in Eqs. (9) and (10). The curve labeling (by color, as well as by dashing and arrowhead filling) corresponds to the right-moving dislocation [see Fig. 2(d)] having the Burgers vector as depicted in the legend at right, where ϕ is measured relative to the cylinder axis $\hat{\boldsymbol{x}}$. Arrowheads in (a) and (b) indicate the direction of the change of helical angle ϕ with each plastic deformation event. Solid curves indicate that the dislocation unbinding increases R, whereas for dotted curves R decreases. For curves with filled arrowheads ($\pm\mathbf{a}_{1,2}$), left-pointing arrowheads correspond to left-pointing unit vectors in the legend, and likewise for right-pointing arrowheads. (a) Axial stress σ_{xx} minus a pressurelike azimuthal stress σ_{yy}, in units of $A = Y/4\pi$. (b) Torsional stress σ_{xy}/A. Note that all dislocation unbinding events in (a), with $(\sigma_{xx} - \sigma_{yy})^\dagger > 0$, decrease the tube radius R.

B. Effects of the bending energy

So far we have neglected the bending energy F_b of the tubular crystal, which we now introduce as

$$F_b = \frac{1}{2}\kappa \int dA[H(\mathbf{x})]^2, \tag{12}$$

where κ is the bending modulus and $H(\mathbf{x})$ is the local mean curvature, equal to the sum of the two principal curvatures of the surface. There could, in general, be another term $\bar{\kappa}K(\mathbf{x})$ associated with the Gaussian curvature $K(\mathbf{x})$, but we restrict our attention to cylinders of infinite length (or with periodic boundary conditions) where the integrated Gaussian curvature vanishes.

Comparing the Young's and bending moduli gives rise to a length scale of local out-of-plane deformation $\sqrt{\kappa/Y}$ at which stretching and bending energies are of comparable magnitude. For cylinders of radius R, therefore, the relative importance of stretching and bending energies is characterized by a dimensionless ratio called the Föppl-von Kármán number

(see, e.g., [48]):

$$\gamma \equiv \frac{YR^2}{\kappa}. \tag{13}$$

For large γ, the tube will prefer to bend to minimize the elastic energy; for small γ, local changes in the lattice constant leading to stretching or compression are the preferred mode of deformation.

How does the bending energy affect the energetics of plastic deformation in a tube? For a pristine tubular crystal in the continuum approximation, with an exactly cylindrical shape of length L and radius R, the bending energy approaches a simple limit,

$$F_b \to \pi\kappa L/R. \tag{14}$$

The bending energy is thus decreased by increasing the cylinder radius and decreasing its length; for glide deformations that keep the number of particles fixed, F_b favors changing m and n to obtain larger $R(m,n) \approx (a/2\pi)\sqrt{m^2+n^2-mn}$. Now consider a tube for which the stretching energy F_s has a local minimum with $L = L_0$ and $R = R_0$. If $\gamma = YR_0^2/\kappa$ is large but finite, we expect a slight increase in radius $R = R_0(1+u_{yy})$, $0 < u_{yy} \ll 1$, and a small decrease in length, $L = L_0(1+u_{xx})$, $u_{xx} < 0$, $|u_{xx}| \ll 1$, where u_{yy} is the azimuthal strain and u_{xx} is the strain along the cylinder axis. Upon expanding in the small quantities $|u_{xx}|$, u_{yy}, and γ^{-1}, we find the total energy of the cylinder,

$$\begin{aligned} F_{\rm tot} &= F_b + F_s \\ &= \frac{\pi\kappa L}{R} + \frac{1}{2}(2\pi RL)\left[2\mu\left(u_{xx}^2+u_{yy}^2\right)+\lambda\left(u_{xx}+u_{yy}\right)^2\right] \end{aligned} \tag{15}$$

$$\begin{aligned} &\approx \pi R_0 L_0\left[Y\gamma^{-1}(1+u_{xx}-u_{yy})\right. \\ &\quad \left.+(2\mu+\lambda)\left(u_{xx}^2+u_{yy}^2\right)+2\lambda u_{xx}u_{yy}\right]. \end{aligned} \tag{16}$$

To first order in γ^{-1}, $F_{\rm tot}$ is minimized by $u_{yy} = -u_{xx} = Y\gamma^{-1}/(4\mu) = \frac{1}{2}(1+\nu)\gamma^{-1}$, where $\nu = \lambda/(2\mu+\lambda)$ is the Poisson ratio [45]. The bending energy therefore acts like a diagonal, traceless, radius-dependent contribution to the stress tensor,

$$\sigma_{yy}^b = -\sigma_{xx}^b = \frac{1}{2}Y\gamma^{-1}, \qquad \sigma_{xy}^b = 0, \tag{17}$$

as can be verified by replacing F_b with $-\int dA\sigma_{ij}^b u_{ij} = -\int dA(\sigma_{yy}^b u_{yy} + \sigma_{xx}^b u_{xx})$ in $F_{\rm tot}$.

How does the bending energy affect the stresses required for plastic deformation by dislocation glide? As seen in Eq. (9), the critical axial stress $\sigma_{xx}^\dagger$ and azimuthal stress $\sigma_{yy}^\dagger$ oppose one another, affecting glide motion only in the combination $(\sigma_{xx}-\sigma_{yy})^\dagger$. We have just found that the bending energy's effective stress contribution has $\sigma_{xx}^b = -\sigma_{yy}^b$. Therefore, the effective critical stress contains a simple "curvature offset,"

$$\begin{aligned} (\sigma_{xx}-\sigma_{yy})_{\rm eff}^\dagger &= (\sigma_{xx}-\sigma_{yy})^\dagger + \left(\sigma_{xx}^b - \sigma_{yy}^b\right) \\ &= (\sigma_{xx}-\sigma_{yy})^\dagger - 4\pi A\gamma^{-1}. \end{aligned} \tag{18}$$

The left-hand side, the effective critical stress to unbind a dislocation pair, must match the critical stress calculated in Eq. (9), which depends on ϕ but not R. Meanwhile, the curvature offset $-4\pi A\gamma^{-1}$ depends on R but not ϕ. The quantity $(\sigma_{xx}-\sigma_{yy})^\dagger$ on the right-hand side of Eq. (18) is the externally imposed stress actually required to unbind a dislocation pair in the presence of a bending rigidity.

For the case of imposed torsional stress, we can obtain a similar curvature-induced stress offset by replacing $(\sigma_{xx}^{\rm ext}-\sigma_{yy}^{\rm ext})$ in Eq. (8) with $(\sigma_{xx}^b-\sigma_{yy}^b) = -4\pi A\gamma^{-1}$ and solving for $\sigma_{xy}^{\rm ext}$ to obtain $(\sigma_{xy})_{\rm eff}$. Setting $r^* = a$ gives a stress offset that now depends on the angle θ that the Burgers vector makes with the cylinder axis,

$$(\sigma_{xy})_{\rm eff}^\dagger = sA/\cos(2\theta) = \sigma_{xy}^\dagger + 2\pi A\gamma^{-1}\tan(2\theta).$$

Upon returning to the case of imposed axial tension, from Fig. 3(a) we see that in order to have a plastic deformation event that decreases R, we need a reduced stress $(\sigma_{xx}-\sigma_{yy})_{\rm eff}^\dagger/A \equiv \tilde{\sigma}_c(\phi)$ between 2 and $4/\sqrt{3} \approx 2.31$, depending on ϕ. By symmetry, if $(\sigma_{xx}-\sigma_{yy})_{\rm eff}/A$ is *negative* but greater in magnitude than the critical value $\tilde{\sigma}_c(\phi)$, then the tube will plastically deform by glide of dislocations that *increase* R. The $+x$-moving dislocation will have Burgers vector opposite to one of those indicated in Fig. 3(a), i.e., the directions coded blue, green, or red (solid-line arrow stems). Equation (18) therefore implies that the bending energy alone is sufficient to destabilize narrow tubes with respect to dislocation unbinding events that increase R, provided γ^{-1} is not too small. Specifically, for a given ratio κ/Y and helical tilt ϕ, there is a critical radius

$$R_c = \sqrt{\frac{4\pi\kappa}{\tilde{\sigma}_c(\phi)Y}}, \tag{19}$$

below which a tube with $R < R_c$ will undergo a plastic deformation event that increases the radius spontaneously, even in the absence of any external stress. (Note that $\sqrt{\kappa/Y}$ must be at least of order $3a/2\pi$ in order for a tube with $R < R_c$ to be a geometrical possibility.)

The curvature corrections calculated above assume that γ^{-1} is small. However, γ^{-1} must still be large enough in order for this effect to be easily observable. Is this the case in single-walled carbon nanotubes? SWCNTs have unit cell spacing $a \approx 0.24$ nm, a 2D Young's modulus of $Y \approx 340\ {\rm J/m^2}$ [22,49,50], and a bending modulus calculated from monolayer graphene to be $\kappa \approx 2\times10^{-19}$ J [51,52]. Thus, $\tilde{\kappa} = \kappa/Ya^2 \approx 0.01$, and $\gamma^{-1} = (a/R)^2\tilde{\kappa}$ is in the range 10^{-3}–10^{-2} for typical carbon nanotubes with $2\pi R/a$ of order 10, suggesting that it would be difficult to measure the effects of the curvature energy in this system.[1] However, a curvature-induced force $\propto \kappa a/R_0^2$ on dislocation pairs has been noted in simulation studies

[1]Thermal fluctuations are known to give rise to renormalized, scale-dependent bending rigidity $\kappa_R(\ell)$ and Young's modulus $Y_R(\ell)$ (where ℓ is the length scale), such that $\kappa_R(\ell)/Y_R(\ell)$ may be greater than κ/Y by a factor $(\ell/\ell_{\rm th})^{\eta-\eta_u}$ [53]. Here $\ell_{\rm th}$ is a thermal length scale $\ell_{\rm th} \propto \sqrt{\kappa^2/(k_BTY)}$ that is approximately 2 nm at room temperature, and $\eta-\eta_u \approx 0.46$. If the nanotube circumference $2\pi R$ is substituted for ℓ, we find that thermal fluctuations give a renormalized reduced bending rigidity $\tilde{\kappa}_R(\ell) \equiv [\kappa_R(\ell)/Y_R(\ell)a^2] \approx c\tilde{\kappa}(R/a)^{0.46}$, where $\tilde{\kappa} = \kappa/Ya^2 \approx 0.01$ and $c = (2\pi a/\ell_{\rm th})^{0.46} \approx 0.88$. Then the renormalized inverse Föppl-von Kármán number

of carbon nanotubes [54]. We note that molecular dynamics simulations of carbon nanotubes have found that, at least for zigzag tubes ($\phi = 30^\circ$, corresponding to parastichy indices $m = n$ in our notation), the formation energy of a dislocation pair may become negative for $n < 14$, although the radius of the $n = 14$ zigzag tube is about an order of magnitude greater than $R_c \approx 0.2a$ [23].

IV. NUMERICAL MODELING

A. Numerical approach

To study how well our continuum elastic predictions apply to tubes of finite size, we now describe numerical simulations of dislocation glide in tubular crystals under axial stress $\sigma_{xx} > 0$. The tubular crystal is modeled as a network of harmonic springs connecting nodes at the sites of a triangular lattice, following Ref. [45]. The initial spring network gives the crystal a tubular topology and a particular choice of phyllotactic indices (m,n), with each node connected to six springs so that the lattice is initially a pristine (defect-free) triangular crystal.

We implement periodic boundary conditions in the X direction, parallel to the cylinder axis $\hat{\mathbf{x}}$ (in the case of a pristine tube), with springs joining nodes across the periodic boundaries. Periodic boundary conditions offer two advantages: We can ignore the complications of end effects for dislocation dynamics, and the Gaussian curvature modulus does not contribute to the energy because the tube has no boundary.

As in Ref. [45], the stretching energy is discretized by defining a spring constant ϵ via a stretching energy

$$F_s^{\text{discrete}} = \frac{1}{2}\epsilon \sum_{\langle j,k \rangle} (|\mathbf{R}_j - \mathbf{R}_k| - 1)^2, \tag{20}$$

which corresponds to Eq. (3) with the choice $\mu = \lambda = \frac{\sqrt{3}}{4}\epsilon$. Here position vectors $\mathbf{R}$ are vectors in $\mathbb{R}^3$, and $\sum_{\langle j,k \rangle}$ is a sum over neighboring nodes connected by an edge within a particular triangulation. The Young's modulus and Poisson ratio are then $Y = \frac{2}{\sqrt{3}}\epsilon$ and $\nu = \frac{1}{3}$, respectively. Simulation lengths are scaled in units of the preferred lattice spacing, equal to the spring rest length. For a discrete version of the bending energy, we use the mean curvature energy discretization from Ref. [55], which can be written

$$F_b^{\text{discrete}} = \kappa \sum_j \frac{\left[\sum_{k(j)} c_{jk}(\mathbf{R}_j - \mathbf{R}_k)\right]^2}{\sum_{k(j)} c_{jk}(\mathbf{R}_j - \mathbf{R}_k)\cdot(\mathbf{R}_j - \mathbf{R}_k)}, \tag{21}$$

where $c_{jk} \equiv \cot\theta_{jk}^1 + \cot\theta_{jk}^2$, and θ_{jk}^i $(i = 1,2)$ are the angles opposite the edge jk in the two faces to which that edge belongs. $\sum_{k(j)}$ is a sum over neighboring nodes k sharing an edge with node j. In the continuum limit, this bending energy corresponds to $F_b = \frac{1}{2}\kappa \int dxdy H^2$, which for a cylinder of length L and radius R reduces to $\pi\kappa L/R$. An alternative curvature energy discretization is [45]

$$F_b^{\text{discrete},2} = \frac{1}{\sqrt{3}}\tilde{\kappa} \sum_{\langle \alpha,\beta \rangle} |\mathbf{n}_\alpha - \mathbf{n}_\beta|^2 = \frac{2}{\sqrt{3}}\tilde{\kappa} \sum_{\langle \alpha,\beta \rangle} (1 - \mathbf{n}_\alpha \cdot \mathbf{n}_\beta), \tag{22}$$

penalizing deviations between the unit normal directions of neighboring faces (summing over all pairs of neighboring faces). We do not use this form because, even though Eq. (22) has the correct continuum limit of $F_b = \frac{1}{2}\kappa \int dxdy(H^2 - 2K)$ for an unstrained lattice, it contains no information about stretching of the triangular faces and therefore does not give the correct scaling $F_b \to \pi\kappa L/R$ for pristine cylinders with periodic boundary conditions under external forces. In contrast, we have checked that the discretization in Eq. (21) for the bending energy converges to $\pi\kappa L/R$ to within 1% for a wide variety of strained and unstrained tubular crystals, including those as small as $R \approx 3a$.

Recall that the lattice sites of a tubular crystal are well approximated by the centers of disks packed in a cylindrical surface. Therefore, we use the latter geometry as an initial state and then minimize the energy over node positions to obtain the preferred lattice sites of the pristine tubular crystal. A dislocation pair is then created from the pristine lattice by a bond flip that removes a bond between neighboring nodes j,k and replaces it with a new bond between nodes j' and k', the common neighbors of j and k, as shown in Figs. 4(a) and 4(b). The node pairs $\{j,j'\}$ and $\{k,k'\}$ are then a pair of dislocations with equal and opposite Burgers vectors, each composed of a positive disclination at a five-coordinated node (j or k) and a negative disclination at a seven-coordinated node (j' or k'). Thereafter, dislocation glide of $\{k,k'\}$ by one lattice spacing to a neighboring node pair $\{\ell,\ell'\}$ is accomplished by a similar bond flip, removing the bond $k'\ell$ and replacing it with a new bond $k\ell'$, as depicted in Fig. 4(c). By repeating this process on either or both dislocations, we can adjust the

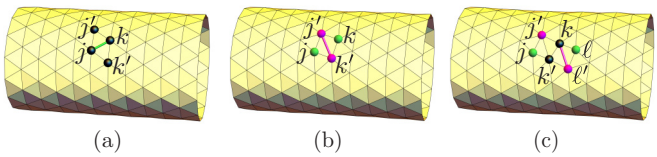

FIG. 4. Illustration of dislocation nucleation and glide by bond flips. (a) In a pristine lattice, with all nodes six-coordinated, a bond jk between nodes j and k, shown as the thick bond in green (medium gray), is chosen to be flipped. (b) Bond jk is replaced with a new bond $j'k'$ in magenta (dark gray) connecting the common neighbors of j and k. This nucleates two dislocations $\{j,j'\}$ and $\{k,k'\}$. Five-coordinated and seven-coordinated disclinations are labeled by green (medium gray) and magenta (dark gray) spheres, respectively. (c) Another bond flip, replacing bond $k'\ell$ with a new magenta (dark gray) bond $k\ell'$, glides the rightmost dislocation from $\{k,k'\}$ to $\{\ell,\ell'\}$; nodes k and k' return to being six-coordinated and are labeled with black spheres.

is $\gamma_R^{-1}(\ell) = (a/R)^2 \times [\kappa_R(\ell)/Y_R(\ell)a^2] \approx 0.88\tilde{\kappa}(R/a)^{-1.54}$ (still with $\ell = 2\pi R$). The result is, at most, a very modest increase in $\gamma_R^{-1}(\ell)$ compared to the zero-temperature value $\gamma^{-1} = \tilde{\kappa}(R/a)^{-2}$. Raising the absolute temperature by a factor of 10 contributes merely a factor of $10^{0.46/2} \approx 1.7$ to γ^{-1}. Therefore, thermal effects are not expected to significantly change the results here.

glide separation distance r of the dislocation pair in discrete steps, always assuming a small but finite temperature ensures enough energy to easily surmount the small Peierls potential.

For each spring network, the total energy $F_{\rm tot} = F_s^{\rm discrete} + F_b^{\rm discrete}$ is minimized over the positions $\{\mathbf{R}_i\}$ of all nodes using a conjugate gradient algorithm from the ALGLIB package [56]. We probe the energy landscape of dislocation glide by comparing $F_{\rm tot}$ for a given dislocation glide separation to $F_{\rm tot}$ with the dislocations one glide step closer together or one step farther apart. The option giving the lowest $F_{\rm tot}$ determines the new state of the system. There are three possible final outcomes: The dislocations may annihilate into the defect-free state; they may reach a separation along the cylinder axis of at least half the length of the perfect cylinder; or they may come to rest at some smaller but nonzero separation. In the case of the second outcome, we consider the dislocations to be "free", i.e., on a truly infinite cylinder we expect they would continue gliding to infinite separation. If the dislocations annihilate or come to rest at a smaller separation, we consider them to be still bound.

Periodic boundary conditions in X require two more independent variables in addition to the node positions: the horizontal length L_X of the box, and a rotation angle β by which the right end of the cylinder is rotated about the $\hat{\boldsymbol{X}}$ axis before being reconnected with the left end. Chiral lattices generically necessitate nonzero values of β. We minimize over L_X and β simultaneously with the node positions $\{\mathbf{R}_i\}$. Before the application of any strain, we record the "rest" values L_X^0 and β^0 of these variables. Then, we can apply an axial strain u_{xx} by holding L_X fixed at $L_X^0(1+u_{xx})$. A torsional strain could be applied by holding β fixed at $\beta^0[1-(L_X/R)u_{xy}]$ [26].

B. Critical stresses and pathways of plastic deformation

The numerical results for plastic deformation under axial tension are plotted in Figs. 5 and 6 for a range of (m,n) initial tubular crystal tessellations. Starting from zero, an applied axial strain is slowly increased in steps of 1%. At small strains, any dislocation pair annihilates immediately after it is nucleated, returning to the pristine lattice. At a critical stress $\sigma_{xx}^{\dagger}$, a dislocation pair with one of the six available Burgers vector pairs unbinds and glides apart to freedom. [For some (m,n) values, two Burgers vectors unbind at the same $\sigma_{xx}^{\dagger}$.] Figure 5 records with colored arrows the plastic deformations $(m,n) \to (m',n')$ obtained in this way, using the Burgers vector coloring scheme introduced in Fig. 2. These arrows collectively indicate the flow through the configuration space of parastichy numbers (m,n) values [or, equivalently, quantized (R,ϕ) values] under axial tension. The overall response to an axial stress $\sigma_{xx} > 0$ is, of course, a step-by-step decrease in R.[2] Meanwhile, there is a convergence of the lattice orientation toward the $m = n$ line of achiral states, where $\phi = 30^\circ$, as predicted in Fig. 3(a). Because of the stepwise nature of the plastic deformation toward smaller R, with $(\Delta m, \Delta n) = (0,-1)$ or $(-1,0)$ at each step, the parastichy tilt angle angle ϕ oscillates slightly about 30° as the tube radius shrinks, as

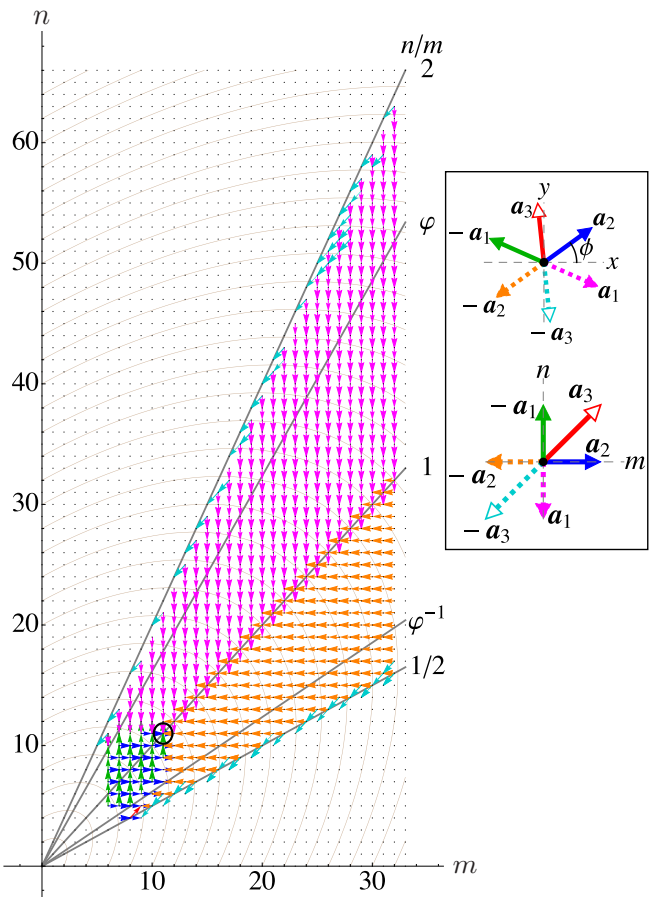

FIG. 5. Numerical results for plastic deformation of tubular crystals, in terms of changes in the parastichy numbers (m,n), under axial tension $\sigma_{xx} > 0$ with a reduced bending modulus $\tilde{\kappa} = \kappa/Ya^2 = 0.5$. The dislocations that unbind at lowest applied stress (consistent with the allowed transitions summarized in Table I) are recorded. Arrows connecting grid points indicate the transformation of the tubular crystal from (m,n) to (m',n'). The arrowhead direction corresponds to the Burgers vector as shown in the lower of the two $\mathbf{a}_i$ legends at right. The color scheme used in Figs. 2 and 3 is repeated here, and the two legends at right show the correspondence of the $\mathbf{a}_i$ orientations in the tube tangent plane (upper legend) with the associated change in the (m,n) parastichy number configuration space (lower legend). Brown (light gray) elliptical contours are curves of constant $R \propto \sqrt{m^2+n^2-mn}$. Lines of constant ϕ (i.e., constant n/m) are shown in medium gray, with n/m as marked on the right side. Here $n/m = 1$ corresponds to $\phi = 30^\circ$. For comparison, we show the golden mean $\varphi = \frac{1}{2}(1+\sqrt{5})$ and its inverse, favored in many instances of plant phyllotaxis [1,2]. Blue (right-pointing), green (upward-pointing), and red (pointing diagonally up, right) arrows are tube-widening events triggered by the bending rigidity that occur at zero applied stress. The point ringed by a black circle marks the widest tube with $m = n$ that is unstable to spontaneous tube-widening dislocation pairs, driven by the bending energy. This gives the critical tube radius $R_c/a \approx 11/(2\pi)$ for $\phi = 30^\circ$ and $\tilde{\kappa} = 0.5$, corresponding to the data point ringed by a black circle in Fig. 7.

[2]Negative σ_{xx} or a torsion σ_{xy} have the additional complications of buckling or supercoiling, instabilities which are outside the scope of this paper.

also found for carbon nanotubes [22]. Plastic deformations with $(\Delta m, \Delta n) = (-1,-1)$, with $\mathbf{b} = -\mathbf{a}_3$ (arrows pointing diagonally down, left, colored cyan), were recorded only near $\phi = 0$ or 60°, where Fig. 3(a) shows that the theoretically

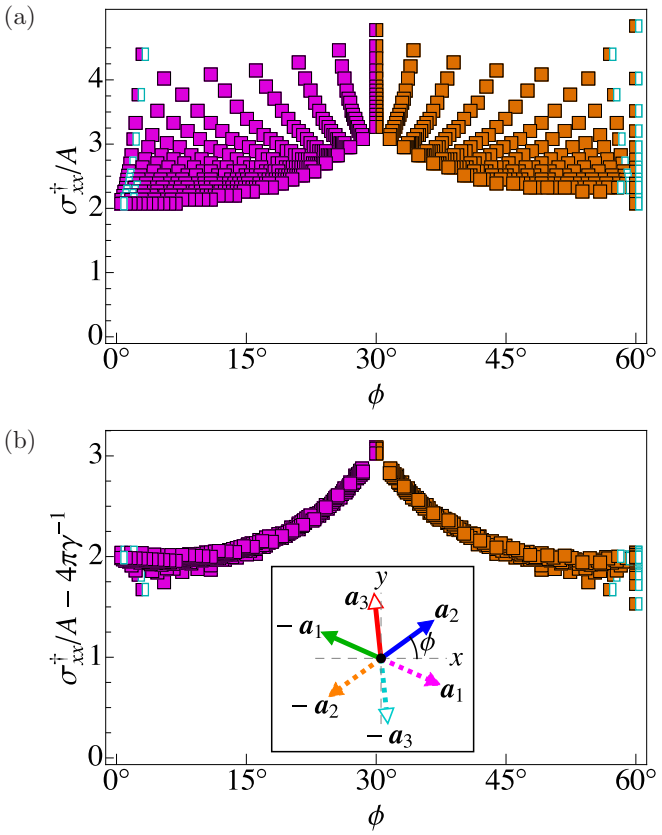

FIG. 6. Numerically calculated critical axial stresses for plastic deformation of tubular crystals with a reduced bending modulus $\tilde{\kappa} = \kappa/Ya^2 = 0.5$, excluding the spontaneous widening deformations at zero applied stress. (a) The critical applied axial stress $\sigma^{\dagger}_{xx}$ required for each dislocation unbinding event in (a) as a function of ϕ, with strings of closely spaced squares swept out as R varies. (b) The same data as in (a) but collapsed by including the curvature correction from Eq. (18). The color scheme for the Burgers vector is the same as in the above figures, with the legend reproduced in the inset to (b). The Burgers vector is $\mathbf{a}_1$ for magenta (dark gray) data points, $-\mathbf{a}_2$ for orange (medium gray) data points, and $-\mathbf{a}_3$ for white data points outlined in cyan (light gray).

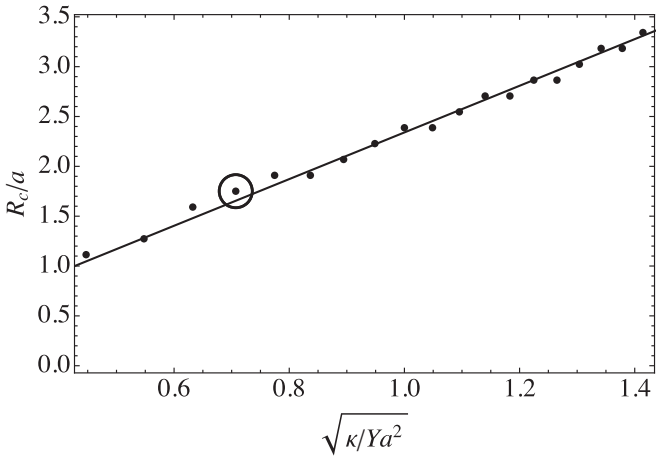

FIG. 7. Critical tube radius R_c, below which bending energy causes spontaneous dislocation unbindings that increase the tube radius (for $m = n$ achiral tubes only), as a function of the curvature modulus κ. The curve is a best fit $R_c = \sqrt{1.74\pi\kappa/Y}$, in good agreement with the prediction $R_c \approx \sqrt{1.73\pi\kappa/Y}$ from Eq. (19) (with $\phi = 30^\circ$). The data point ringed by a black circle corresponds to the circled $(m,n) = (11,11)$ grid point in Fig. 5.

predicted $(\sigma_{xx} - \sigma_{yy})^{\dagger}$ for $\mathbf{b} = -\mathbf{a}_3$ coincides with the minimal $(\sigma_{xx} - \sigma_{yy})^{\dagger}$ associated with $\mathbf{a}_1$ or $-\mathbf{a}_2$.

The critical axial stress $\sigma^{\dagger}_{xx}$ required to pull apart the dislocations recorded in Fig. 5 is plotted in Fig. 6(a) as a function of ϕ. In Fig. 6(b), the data collapses to a single curve when the curvature offset to σ_{xx} due to the final bending rigidity term in Eq. (18) is included. The scatter in Fig. 6(a) reflects the R dependence of $\sigma^{\dagger}_{xx}$, but Fig. 6(b) confirms that the R dependence is described simply by the curvature offset $-Y\gamma^{-1} = -\kappa/R_0^2$, where R_0 is the radius that minimizes the stretching energy F_s. With this correction, the critical stress depends only on ϕ. While Figs. 5 and 6 show results for reduced bending modulus $\tilde{\kappa} \equiv \kappa/Ya^2 = 0.5$, similar results were obtained for $\tilde{\kappa} = 0.25$, 0.75, and 1. The Burgers vectors and the magnitude of $\sigma^{\dagger}_{xx,\mathrm{eff}}$ in Fig. 6(b) are in approximate agreement with the predictions of Fig. 3(a). However, the exact shape of the $\sigma^{\dagger}_{xx,\mathrm{eff}}$ curve as a function of ϕ differs somewhat between theory and numerics, reflecting differences between the continuum and discrete formulations.

An interesting feature of Fig. 5 is the presence of green (pointing up), blue (pointing right), and red (pointing diagonally up, right) arrows at small R, indicating plastic deformation events that increase R, contrary to the predominant magenta (pointing down), orange (pointing left), and cyan (pointing diagonally down, left) arrows that all show the tube radius shrinking. These tube-widening deformations occur at zero applied axial strain and arise solely from the effective stresses σ^{b}_{xx} and σ^{b}_{yy} generated by the bending energy as given in Eq. (17). As predicted, there is a critical radius R_c below which the bending energy alone makes narrow tubes unstable to widening. To compare quantitatively with theory, we fixed $\phi = 30^\circ$ and varied $m = n \approx 2\pi R/a$ to find the largest radius R_c at which a tube-widening deformation occurs spontaneously. This procedure was repeated over a range of values of the reduced bending modulus $\tilde{\kappa} \equiv \kappa/Ya^2$. The results are plotted in Fig. 7, which shows that R_c/a varies as $\sqrt{\tilde{\kappa}}$. A linear fit gives $R_c = \sqrt{1.74\pi\kappa/Y}$, which agrees well with the prediction in Eq. (19), $R_c \approx \sqrt{1.73\pi\kappa/Y}$, using $\tilde{\sigma}_c(\phi = 30^\circ) = 4/\sqrt{3}$.

C. Tube axis reorientation by dislocations

The simulated tubes reveal that, in the presence of dislocations, the deviations from a perfect cylindrical shape are not limited to changes in radius: In addition, the dislocations create kinks in the tube axis, as can be seen in Figs. 8(a) and 8(b). As pointed out in Ref. [17], a pair of dislocations in a crystal on a perfectly cylindrical surface acts like a pair of grain boundaries, between which the crystal axes are slightly reoriented. We find that when the tubular crystal is free to assume an energy-minimizing shape, it is approximately piecewise cylindrical (far from the transition regions discussed in the following section) with a kink angle in the tube axis

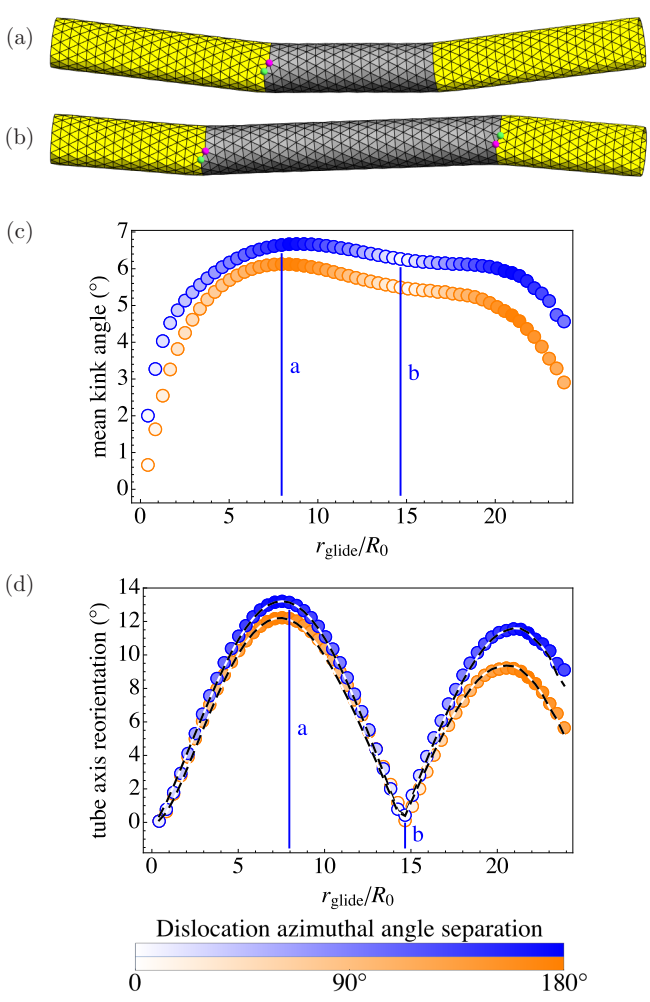

FIG. 8. Tube axis reorientation in the presence of dislocations. (a),(b) Two snapshots from the glide process of a simulated tubular crystal undergoing a plastic deformation from $(m,n) = (15,15)$ in yellow (light gray) to $(m',n') = (15,14)$ in dark gray, with reduced bending rigidity $\kappa/Ya^2 \equiv \tilde{\kappa} = 0.09$. Green (medium gray) and magenta (dark gray) spheres indicate the dislocations' five- and seven-coordinated disclinations, respectively. The rightmost dislocation is on the far side of the tube in (a). The external stress is set to zero at each snapshot. (c) Plot of the tube axis kink angle, averaged over the two dislocation sites, as a function of the dislocations' glide separation distance in units of the initial tube radius R_0. (d) The angle between the leftmost and rightmost segments of the tube axis, measuring reorientation of the tube axis by the (m',n') region, as a function of dislocation glide separation distance. Dashed black-and-white curves are the geometric model for tube axis reorientation as given in Eq. (24). In both (c) and (d), blue (upper) and orange (lower) data points correspond to reduced bending modulus $\tilde{\kappa} = 0.09, 0.9$, respectively, and vertical blue lines correspond to snapshots (a) and (b), as indicated. Color saturation of data points indicates the dislocations' azimuthal angle separation, as shown in the legend at bottom, where blue (upper) and orange (lower) color bars correspond to blue (upper) and orange (lower) data sets in (c) and (d).

associated with a reorientation of the crystal axes across the boundaries between the different (m,n) tessellations. Thus, while one pair of dislocations is gliding apart, the tube axis contains two kinks at the boundaries between the outer (m,n) and inner (m',n') tessellations. Here we approximate the tube axis using a computed "spine curve" as described in the next section. We also remove the periodic boundary conditions along the tube axis to investigate the bending of tubes by dislocations. After each glide step, the applied strain is set to zero and the tube conformation is relaxed with the dislocations frozen in place.

Averaging over the two tube axis kinks, we find a kink angle on the order of $a/|\mathbf{C}|$, or (equivalently) of the difference $\Delta\phi$ between the helical orientations of the two tessellations, provided that the dislocation separation r_{glide} exceeds the circumference $\approx 2\pi R_0$. This average kink angle is plotted in Fig. 8(c) as a function of r_{glide} for a $\mathbf{b} = \pm\mathbf{a}_1$ dislocation pair during the plastic deformation process $(m,n) = (15,15) \rightarrow (m',n') = (15,14)$. Because the dislocations move along their helical glide paths, the azimuthal angle separation of a defect pair [shown as color saturation of data points in Figs. 8(c) and 8(d)] varies linearly with r_{glide}. Blue (upper) and orange (lower) data points correspond, respectively, to reduced bending modulus $\tilde{\kappa} = 0.09, 0.9$, showing that there is only a weak dependence of this effect on $\tilde{\kappa}$. Figures 8(a) and 8(b) are snapshots from the $\tilde{\kappa} = 0.09$ case.

The net effect of the pair of kinks on the tube axis orientation depends crucially on the relative azimuthal coordinates of the two dislocations. If the two dislocations are on opposite sides of the tube, as in Fig. 8(a), their respective kink angles add constructively, effectively bending the tube. In contrast, if the two dislocations are on the same side of the tube, as in Fig. 8(b), the two kinks effectively cancel each others' reorientations of the tube axis, producing a tube conformation that is not bent but instead zigzagged. Figure 8(d) shows the angle between the tube axis in the left (m,n) region and the tube axis in the right (m,n) region, i.e., the change in tube axis orientation after traversing the (m',n') region. The data is again plotted as a function of dislocation pair glide separation r_{glide} and shows only a weak dependence on $\tilde{\kappa}$. The tube axis reorientation angle is near its maximum in Fig. 8(a) and nearly zero in Fig. 8(b), with intermediate azimuthal separation angles of the defects producing states intermediate between the bent and zigzagging tube conformations.

We can understand the shapes of the tube reorientation angle curves in Fig. 8(d), producing the dashed black-and-white line approximations shown there, through the following geometric reasoning. Assume that the tube axis $\hat{\boldsymbol{t}}_C$ in the central region is along $\hat{\boldsymbol{X}}$ and that each of the two dislocations causes a deflection in the tube axis by a small angle δ in the direction $\hat{\boldsymbol{X}} \times \hat{\boldsymbol{\rho}}$. Here $\hat{\boldsymbol{\rho}}$ is the unit radial vector pointing from the tube axis to the dislocation (see Fig. 10). Then the tube axis on the left side of the tube has unit tangent vector $\hat{\boldsymbol{t}}_L \propto \hat{\boldsymbol{X}} + \delta(\hat{\boldsymbol{X}} \times \hat{\boldsymbol{\rho}}_L)$, and likewise on the right side of the tube $\hat{\boldsymbol{t}}_R \propto \hat{\boldsymbol{X}} + \delta(\hat{\boldsymbol{X}} \times \hat{\boldsymbol{\rho}}_R)$, where $\hat{\boldsymbol{\rho}}_L$ and $\hat{\boldsymbol{\rho}}_R$ correspond, respectively, to the left and right dislocations. For a dislocation at azimuthal angle coordinate α relative to $\hat{\boldsymbol{Y}}$, we have $\hat{\boldsymbol{X}} \times \hat{\boldsymbol{\rho}} = \hat{\boldsymbol{Z}} \cos\alpha - \hat{\boldsymbol{Y}} \sin\alpha$. After normalizing $\hat{\boldsymbol{t}}_L$ and $\hat{\boldsymbol{t}}_R$, it is straightforward to determine that

$$\hat{\boldsymbol{t}}_L \cdot \hat{\boldsymbol{t}}_R = \frac{1 + \delta^2 \cos(\Delta\alpha)}{1 + \delta^2}, \tag{23}$$

where $\Delta\alpha$ is the difference in azimuthal angular coordinate α between the dislocations. Setting Eq. (23) equal to $\cos\omega$,

where ω is the (small) tube axis reorientation angle, we find

$$\omega \approx \delta\sqrt{2[1-\cos(\Delta\alpha)]}. \tag{24}$$

In Fig. 8(d), at each data point we use for the deflection angle δ the numerically measured mean kink angle from Fig. 8(c). The dislocations' azimuthal separation $\Delta\alpha$ increases linearly with glide separation r_{glide}, with slope determined by the helical pitch of the associated parastichy. The tube axis reorientation angle ω is then calculated using Eq. (24), producing the dashed black-and-white lines in good agreement with the reorientation angle measured directly from the simulated tubes.

V. TUBE TRANSITION REGIONS

So far our analytic calculations have assumed that the tube has a perfect cylindrical or piecewise cylindrical shape, albeit with a radius that can change in time in response to external stress. However, at any intermediate stage of the dislocation pair's glide separation, the radius necessarily changes *spatially* at a pair of transition regions in the tube, where the two dislocations interpolate between regions with different preferred circumferences $|\mathbf{C}(m,n)|$. Given the stepwise nature of the plastic deformation mechanism, the fractional change in radius mediated by each dislocation is typically small, so the cylindrical shape is a reasonable starting approximation. On the other hand, we can use the fractional change in radius as a small parameter, allowing some analytic insight into the equilibrium shape of a tubular crystal interrupted by dislocations, as discussed below. (How these small deviations modify the energy landscape of dislocation motion during plastic deformations is a more subtle problem that we leave for future work.)

In this section, we first apply a local measure of the tubular crystal's radius to compute the profile of the tube's transition region in the numerical simulations. We then compare these results with an analytic treatment of small deflections in thin-walled cylinders.

A. Numerically calculated radius profiles in the transition regions

Defining a local radius for the simulated tube is somewhat subtle. For the tubes shown in Figs. 9(e) and 9(f), isolated dislocations cause slight bending or reorientation of the tube axis (as we have seen in the previous section), which complicates the determination of a centerline from which to measure the radius on the tube surface. To define a tube centerline, or "spine," we adopt the following method: We fix X (the coordinate along the unperturbed cylinder's axis), and then we find the Y and Z coordinates (in $\mathbb{R}^3$) of a point on the spine by finding the zero of a fictitious repulsive force exerted by every lattice site in the tubular crystal on the spine point (with the X component of the force projected out). We found it convenient to impose a fictitious force pointing along the separation direction $\mathbf{d}$ between a tube lattice site and the spine point and varying like $1/|\mathbf{d}|^8$. In tests on point sets sampled from analytically defined canal surfaces [57], this procedure produced a computed spine in good agreement with the known spine curves of these continuous surfaces. Linear interpolation was then used to fill in the spine after a certain number of points

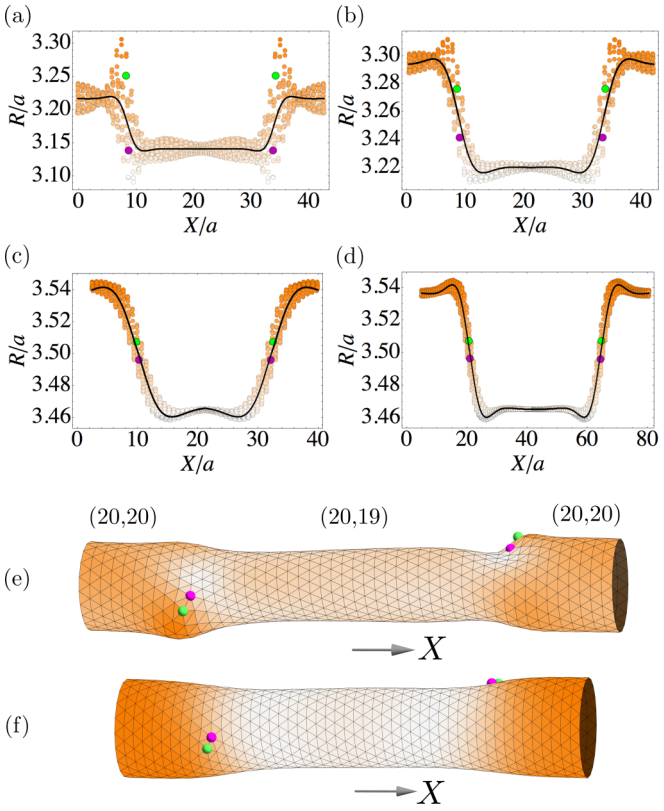

FIG. 9. (a)–(d) Tube radius as a function of coordinate X along the axis of the unperturbed cylinder (both in units of a), as a dislocation pair whose right-moving dislocation has Burgers vector $\mathbf{b} = \mathbf{a}_1$ interpolates between an $(m,n) = (20,20)$ tessellation on the left and right sides and an $(m,n) = (20,19)$ tessellation in the middle. Green (medium gray) and magenta (dark gray) larger dots mark X coordinates of the 5- and 7-coordinated disclinations; color saturation of other data points is a proxy for the local tube radius R. The reduced bending rigidity $\tilde{\kappa} = \kappa/Ya^2$ is 0.1 (a), 0.5 (b), or 2 (c),(d), while the number of lattice sites is $N = 1000$ (a)–(c) or $N = 2000$ (d). The spread in radii at a given X/a is due to the azimuthal variation in the distance to the spine. Theoretical curves (black) are from Eqs. (31)–(35). (e) A heat map of the local radius on the tubular crystal corresponding to (a), with the color saturation corresponding to the R values as shown there, and positive and negative disclinations shown as green (medium gray) and magenta (dark gray) spheres, respectively. (f) A similar heat map of the local radius corresponding to (c). In both (e) and (f), radius variations in the positions of plotted surface points, relative to an average-radius reference cylinder, have been exaggerated by a factor of 10 for clarity.

had been calculated in this way. The local radius at a particular tube lattice site was then estimated as the distance from that site to the nearest point on the calculated spine.

Computed local radius results are shown in Fig. 9 for an intermediate stage in the plastic deformation $(m,n) = (20,20) \rightarrow (20,19)$ by a dislocation pair whose right-moving dislocation has Burgers vector $\mathbf{b} = \mathbf{a}_1$. (Here the axial strain is set to zero before measuring the radius profile.) Three different values of the reduced bending modulus $\tilde{\kappa} = \kappa/Ya^2$ are used in Figs. 9(a)–9(d). R is plotted against X (the coordinate in $\mathbb{R}^3$ most closely aligned with the cylinder axis), suppressing the azimuthal coordinate. For the largest tested

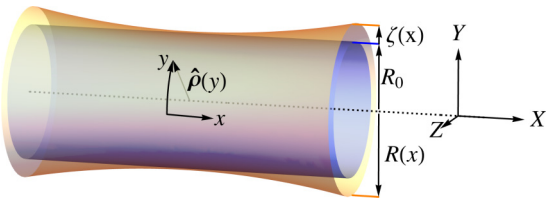

FIG. 10. Schematic illustration of the coordinate systems and variables used in Sec. V to describe a weakly distorted cylinder. An ideal cylinder in blue (inner surface) of radius R_0 is transformed into a surface of revolution in orange (outer surface) with azimuthally symmetric but x-dependent radius $R(x) = R_0 + \zeta(x)$. Lowercase (x,y) are coordinates in the undeflected cylindrical reference surface, respectively, along the axial and azimuthal directions. Uppercase (X,Y,Z) are coordinates of the three-dimensional embedding, with the tube axis (dotted line) oriented along $\hat{\boldsymbol{X}}$. The $\hat{\boldsymbol{\rho}}(y)$ direction points radially out from the tube axis in three dimensions.

bending modulus $\tilde{\kappa} = \kappa/Ya^2 = 2$ in Figs. 9(c) and 9(d), R is approximately independent of the azimuthal coordinate, whereas for small $\tilde{\kappa}$ there is considerable azimuthal variation in R. In Fig. 9(a), where $\tilde{\kappa} = 0.1$, the disclination pairs comprising the dislocations create sharp local disturbances in R, with the positive disclination at a higher R and the negative disclination at a lower R than the radius of either the initial or final pristine tubes. In contrast, at larger $\tilde{\kappa}$ the disclinations do not generate a large local change in R, instead following the gentler slope of the transition region [Figs. 9(c) and 9(d)]. The shift between these two extremes is gradual as $\tilde{\kappa}$ changes, as illustrated in Fig. 9(b) for $\tilde{\kappa} = 0.5$.

The large jump in R between the disclinations at low $\tilde{\kappa}$ in Fig. 9(a) can be understood in light of the known buckling behavior of a membrane with a dislocation. In Ref. [45], a membrane with a dislocation in its center and lattice spacing a was found to buckle, with a sudden jump in the out-of-plane direction between the two disclinations, when the membrane's linear size exceeded $(127 \pm 10)a\tilde{\kappa}$. Upon setting this linear size equal to $2\pi R_0$, we find a critical value $\tilde{\kappa}_b \approx 2\pi R_0/(127a)$ below which buckling is expected. For the $(m,n) = (20,20)$ tube, $\tilde{\kappa}_b \approx 0.16$, in agreement with the buckled behavior we see with $\tilde{\kappa} = 0.1$.

B. Analytic description of radius profiles in the transition regions

We now seek analytic insight into the shape of the transition region in the opposite limit where $\tilde{\kappa} \gg \tilde{\kappa}_b$ and there is a well-defined "transition region profile" $R(X)$. In particular, we would like to understand why $R(X)$ in Figs. 9(b)–9(d) exhibits oscillatory behavior in addition to an overall rise or decay between the narrower and wider region of the tube.

Consider weak radial deflections from a perfect cylinder of radius R_0, described by a function $\mathbf{r}(x,y)$ in $\mathbb{R}^3$,

$$\mathbf{r}(x,y) = [R_0 + \zeta(x,y)]\hat{\boldsymbol{\rho}}(y) + x\hat{\boldsymbol{X}}, \tag{25}$$

where we define a reduced tube deflection $\tilde{\zeta}(x,y) \equiv \zeta(x,y)/R_0 \ll 1$ and $\hat{\boldsymbol{\rho}}(y)$ is the unit radial vector $\hat{\boldsymbol{Y}}\cos(y/R_0) + \hat{\boldsymbol{Z}}\sin(y/R_0)$. These coordinates and variables are illustrated in Fig. 10. The mean curvature for this parametrization is

$$H \approx \zeta_{xx} + \zeta_{yy} - R_0^{-1}(1 - \zeta R_0^{-1}) - 2\zeta\zeta_{yy}R_0^{-1}, \tag{26}$$

where subscript x,y denote spatial derivatives. As seen in Figs. 9(c) and 9(d), for larger $\tilde{\kappa}$ the radius is approximately independent of the azimuthal coordinate. In this regime we can therefore make the simplifying assumption that ζ has no dependence on y. Then

$$H = \zeta_{xx} - R_0^{-1}(1 - \zeta R_0^{-1}). \tag{27}$$

We can estimate the width w of the transition region along the cylinder axis using scaling arguments: Assume that over the transition region width w, there is a change in radius $\Delta\zeta$ of order a, since $R_0 \approx (a/2\pi)\sqrt{m^2 + n^2 - mn}$ and each dislocation changes m and/or n by at most ± 1. The stretching energy density is then $\sim Y(a/R)^2$. The leading-order term in the squared mean curvature is $\zeta_{xx}^2 \sim (a/w^2)^2$, giving a curvature energy density $\sim\kappa(a/w^2)^2$. (Other terms in H^2 are smaller by factors of w/R, which is small, as shown below.) Equating the bending and stretching energy density scalings gives $w \sim \gamma^{-1/4}R$, similar to deformations on a sphere [58]. Thus, w/R scales like the inverse fourth root of the Föppl-von Kármán number γ, and we have assumed γ is large. (See also Ref. [43], where a point force f is applied normal to a thin shell of thickness h, and the shell is deformed by a height $\zeta \sim fR/Yh$, over a region of size $d \sim \sqrt{hR} \sim \gamma^{-1/4}R$.) In contrast, large-amplitude "pinch in a pipe" studied by Mahadevan *et al.* [59] has a persistence length $l_p \sim \gamma^{1/4}\sqrt{R\delta_R}$, where the amplitude of the pinch is δ_R.

To go beyond scaling arguments, we square the mean curvature in Eq. (27) and expand the free-energy density as

$$f = \frac{\kappa}{2}\left[\zeta_{xx}^2 + \frac{\zeta^2}{R_0^4} - \frac{2\zeta_{xx}}{R_0} + \frac{2\zeta_{xx}\zeta}{R_0^2} - \frac{2\zeta}{R_0^3}\right] + \frac{3}{4}Y\frac{\zeta^2}{R_0^2}. \tag{28}$$

The term proportional to Y is the stretching energy due to the strain u_{yy} from the radius differing from the preferred radius R_0, with $\mu = \lambda$ and with the assumption that $u_{xx} = -u_{yy}$, as was found to be the case for perfect cylinders in Sec. III.

The Euler-Lagrange equation associated with Eq. (28) reads

$$0 = \frac{\delta f}{\delta\zeta} = \kappa\left[\zeta_{xxxx} + \zeta R_0^{-4} + 2\zeta_{xx}R_0^{-2} - R_0^{-3}\right] + \frac{3}{2}Y\zeta R_0^{-2} \tag{29}$$

$$\Rightarrow R_0 = R_0^4\zeta_{xxxx} + 2R_0^2\zeta_{xx} + \zeta\left(1 + \frac{3}{2}\gamma\right). \tag{30}$$

Suppose that the transition region is centered on a dislocation at $x = 0$. For $x > 0$, we have a tubular lattice tessellation where the stretching energy prefers a radius R_0^+, and the Föppl-von Kármán number is $\gamma^+ = \tilde{\kappa}(R_0^+/a)^{-2}$. For $x < 0$, the different preferred tubular radius introduces similar parameters R_0^-, γ^-. We now solve Eq. (30) for $x > 0$, subject to boundary conditions $\zeta'(x \to \infty) = \zeta''(x \to \infty) = 0$ and $[R_0^+ + \zeta(x \to \infty)] = R_\infty^+$, where $R_\infty^+ = R_0^+[1 + [1 + \frac{3}{2}\gamma^+]^{-1}] \approx R_0^+[1 + \frac{2}{3}(\gamma^+)^{-1}]$ is the radius of the pristine tubular crystal with this tessellation. Keeping only real solutions, we find

$$R(x>0) = R_0^+ + \zeta(x>0) = R_\infty^+ + c^+ \mathrm{Re}[e^{-x/w^+}], \quad (31)$$

$$w^+ = R_0^+\left[-1 + i\sqrt{\tfrac{3}{2}\gamma^+}\right]^{-1/2}, \quad (32)$$

where the complex number w^+ describes a combination of exponential and oscillatory behavior of $\zeta(x)$, and c^+ has yet to be determined. In the large γ^+ limit, $R(x>0) \to R_\infty^+ + c^+ \exp(-x/v^+)\cos(x/v^+)$, where $v^+ = \sqrt{2}R_0^+(\frac{3}{2}\gamma^+)^{-1/4}$.

At $x = 0$, Eq. (31) must match onto

$$R(x<0) = R_0^- + \zeta(x<0) = R_\infty^- + c^- \mathrm{Re}[e^{x/w^-}], \quad (33)$$

$$w^- = R_0^-\left[-1 + i\sqrt{\tfrac{3}{2}\gamma^-}\right]^{-1/2}. \quad (34)$$

Ensuring that both $R(x)$ and $R'(x) = \zeta'(x)$ are continuous at $x = 0$ requires

$$c^+ = \left(1 + \frac{\mathrm{Re}[1/w^+]}{\mathrm{Re}[1/w^-]}\right)^{-1}(R_\infty^- - R_\infty^+), \quad (35)$$

and a similar expression for c^- with the $^-$ and $^+$ labels reversed.

Equations (31)–(35) are compared to the numerically calculated radius data in Figs. 9(a)–9(d) (black curves); our analytic shape profiles provide reasonably good descriptions of the transition region provided $\tilde{\kappa} \gg \tilde{\kappa}_b$. For the pristine tube radii R_∞^-, R_∞^+, we use radii calculated numerically for defect-free tubes with the associated (m,n); these numerically calculated radii differ slightly ($< 1\%$) from the theoretical values $R_\infty = R_0[1 + (1 + \frac{3}{2}\gamma)^{-1}]$ expected from Eq. (30). (Note that Eq. (1), which defines R_0, is exact for a triangular packing of disks in a cylindrical surface, but is only approximate for a tubular crystal of spheres [10,16].) The real part of the complex parameter $w^\pm$ successfully captures the width of the transition region, and its imaginary part predicts the oscillatory behavior observed in $R(x)$. As predicted by the scaling argument, for large γ the transition region width scales as $w \sim \gamma^{-1/4}R_0$. However, even in that limit, w has a complex prefactor resulting in both exponential rise or decay and oscillations in $R(x)$, controlled by the same length scale.

If the two dislocations are not far apart compared to $\mathrm{Re}[w] \sim \gamma^{-1/4}R_0$, then the two calculated transition region profiles may overlap significantly. The actual $R(x)$, in order to remain smooth, must compromise between the two transition region profiles; we expect this effect leads to small changes in the energetics of dislocation unbinding compared to the calculations in Sec. III.

In this paper we have ignored the interactions between dislocations and the Gaussian curvature $K(\mathbf{x})$ that they induce on a tube. These interactions are described by an energy

$$F_G = \frac{Y}{2}\int dA \int dA'[S(\mathbf{x}) - K(\mathbf{x})]\frac{1}{\Delta^2_{\mathbf{x}\mathbf{x}'}}[S(\mathbf{x}') - K(\mathbf{x}')], \quad (36)$$

where the effective disclination density associated with a dislocation positioned at $\mathbf{x}_b$ is $S(\mathbf{x}) = \epsilon_{ij}b_i\partial_j\delta(\mathbf{x},\mathbf{x}_b)$ and $1/\Delta^2_{\mathbf{x}\mathbf{x}'}$ is the Green's function of the biharmonic operator [60]. The dislocations evidently position themselves near rings on the tube where $R(x)$ has an inflection point and the local Gaussian curvature is approximately zero. As the dislocations glide, the transition regions move with them, such that the contribution of Eq. (36) to the total energy remains approximately constant. The good agreement between Eqs. (31)–(35), which neglect the couplings in Eq. (36), and the numerically calculated transition region profile in Figs. 9(b)–9(d) suggests that the essential role of the dislocations is in switching the preferred radii between R_0^+ and R_0^-, not their coupling to the Gaussian curvature field.

C. Dislocation orientation in the transition regions

Examining the Gaussian curvature K near the transition region reveals an interesting agreement between the energetically preferred dislocation orientation and the geometrical view of dislocation motion in tubular crystals. Five-coordinated disclinations prefer positive K, while seven-coordinated disclinations prefer negative K. Dislocations on Gaussian bumps, for example, prefer to sit near the ring of $K = 0$, oriented with the positive disclination closer to the top of the bump, where $K > 0$, and the negative disclination at larger distance, where $K < 0$ [60]. In our system, a transition region where a tube changes from a larger to a smaller radius has positive K on the wider side of the transition region and negative K on the narrower side of the transition region, as shown in Fig. 11. Thus, a dislocation will energetically prefer to orient with the five-coordinated disclination closer to the wider side. This expectation agrees with the geometry of dislocation motion in a tubular crystal: If a dislocation's positive fivefold disclination is at, say, a larger x coordinate than the negative sevenfold disclination, then the Burgers vector $\mathbf{b}$ has a negative component along the $\hat{\mathbf{y}}$ direction, meaning that the circumference decreases as the dislocation moves in the positive x direction. This dislocation orientation is shown schematically in Fig. 11; see also the rightmost dislocation in the simulated tubular crystals of Figs. 1(e) and 1(f) and in Fig. 2(d). Thus, the positive disclination is closer to the wider side of the tube and will be on the part

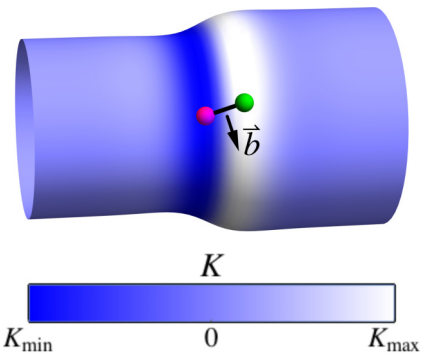

FIG. 11. Schematic illustration of Gaussian curvature K on a tube with a dislocation. At the transition region where the tube radius changes, the Gaussian curvature is mostly positive on the wider side and mostly negative on the narrow side. The dislocation that causes this transition region has its fivefold disclination (green, rightmost sphere) near the ring of maximum K and its sevenfold disclination (magenta, leftmost sphere) near the ring of minimum K.

of the transition region with positive K, while the negative disclination is on the narrower side in a region of $K < 0$, consistent with our simulations.

VI. CONCLUSIONS

We have examined the plastic deformation of tubular crystals by glide of separating dislocation pairs through both continuum elastic calculations and simulations of a discretized harmonic solid sheet with a bending energy wrapped into a tube. Dislocation pairs gliding apart mediate stepwise parastichy transitions, changing the parastichy numbers (m,n) by ± 1 and thus also changing the tube radius R and helical angle ϕ according to Eqs. (1) and (2). The predictions of continuum elasticity calculations offer valuable insights into the numerically calculated mechanics of tubes even when the tube circumference is as small as $\sim$10 times the lattice spacing.

Tubes under axial elongation stress change their lattice structure to converge toward the stable $m = n$ achiral state while their radius shrinks. In the regime where the inverse Föppl-von Kármán number γ^{-1} is small but finite, the bending modulus κ shifts the critical stress required to drive apart dislocations, strengthening narrow tubes against plastic deformations caused by axial stress. By properly correcting the yield stress $\sigma_{xx}^{\dagger}$ required to unbind a dislocation pair with a curvature-induced stress offset $-Y\gamma^{-1} = -\kappa/R^2$, we obtain an effective yield stress as a function of ϕ that is independent of R. If κ is large enough, very small tubes with $R < R_c \propto \sqrt{\kappa/Y}$ may even be unstable to emission of dislocation pairs that widen the tube, driven by the curvature energy alone.

We have focused on positive extensional stresses because compressional stresses ($\sigma_{xx} < 0$) are complicated by the possibility of an Euler buckling transition. Similar buckling phenomena can complicate the response to a torsional stress σ_{xy} of either sign. Both problems are interesting areas for future investigation.

Dislocations at finite separation were found to cause kinks in the tube axis orientation, creating nontrivial tube geometries. The net effect of a pair of kinks on the tubular crystal is determined in large part by their azimuthal angular separation: Bent tubes are formed by dislocations on opposite sides of the tube, whereas zigzagging tube conformations are produced by dislocations on the same side of the tube. Tube geometries intermediate between these extremes may be produced by other angular separations.

We have also examined how the tube radius changes spatially in the transition region surrounding a dislocation. At small reduced bending modulus $\tilde{\kappa} = \kappa/Ya^2$ the simulated tubular crystals show buckling behavior like that observed in simulated crystalline membranes. For larger $\tilde{\kappa}$, the radius varies smoothly as a function of the cylinder's axial coordinate. The transition region has width $w \sim \gamma^{-1/4} R_0$ along the tube axis direction and also exhibits damped oscillations in $R(x)$ at the same length scale, with the dislocation positioned near a ring of zero Gaussian curvature wrapped around the tube.

Our results suggest several additional avenues for fruitful future investigation. One is to examine parastichy transitions at finite temperature, where dislocation pairs form and unbind at rates depending on an escape energy barrier [17]. Another is to consider the response of the tube to bending, which may stabilize dislocations at nonzero, finite separation [38]. Some preliminary observations about bending are presented in the Appendix, where we show that bending a tubular crystal into a torus causes spontaneous unbinding and separation of certain dislocation pairs, provided that the torus's aspect ratio is large enough.

Finally, nontrivial tube conformations could be targeted by the placement of frozen-in defects, as suggested by the numerically observed kinks in the tube axis at the sites of dislocations (Fig. 8). Patterns of defects are expected to promote controllable zigzagging and bending tube shapes. Even more pronounced distortions will be triggered if the disclinations comprising a dislocation separate and migrate to opposite sides of the tube. In the long term, we hope that improved understanding of the mechanics of dislocation-mediated parastichy transitions will aid in the design of mechanically reconfigurable bulk materials or nanomachines.

ACKNOWLEDGMENTS

The authors thank A. Amir, E. Efrati, A. Azadi, and A. Dinsmore for helpful discussions. This work was supported by the National Science Foundation through Grant No. DMR-1306367 and through the Harvard MRSEC Grant No. DMR-1420570. D.A.B. was supported by Harvard University through the George F. Carrier Postdoctoral Fellowship. This research was also supported in part by the National Science Foundation under Grant No. NSF PHY11-25915. The authors thank the Kavli Institute for Theoretical Physics for its hospitality while this work was being discussed and prepared for publication.

APPENDIX: TOROIDAL TUBULAR CRYSTALS

In addition to axial extension and torsion, another type of deformation likely to be encountered by tubular crystals is bending. A uniformly bent rod experiences extension along the outer half and compression along the inner half [43]. Our focus in this paper on tubes with periodic boundary conditions along the tube axis and under uniformly applied stresses precludes a full treatment of dislocation motions in response to general bending forces. However, some insights arise from the special case of the torus tessellated with a tubular crystal. Rather than placing the simulated tubular crystal in a box that is periodic along the X direction, we embed the same bond network tessellation on a torus in $\mathbb{R}^3$. Any tubular crystal with parastichy numbers (m,n) can be mapped onto a physical torus, provided that the torus's major radius R_M is large enough compared to the tubular crystal's radius R to avoid self-intersection. For example, Fig. 12(a) shows a pristine tubular crystal with $(m,n) = (14,18)$ embedded as a torus. Here $2\pi R_M$ is analogous to the length L_X of the periodic box for cylindrical tubular crystals. Such toroidal crystals are in fact sometimes formed by single-walled carbon nanotubes [61,62]. Rather than imposing external stresses, we observe spontaneous dislocation motion in response to the extensional and compressional strains naturally present in the outer and inner portions of the torus, respectively.

A strong bending rigidity is necessary to maintain an approximately circular cross section for the toroidal tubular

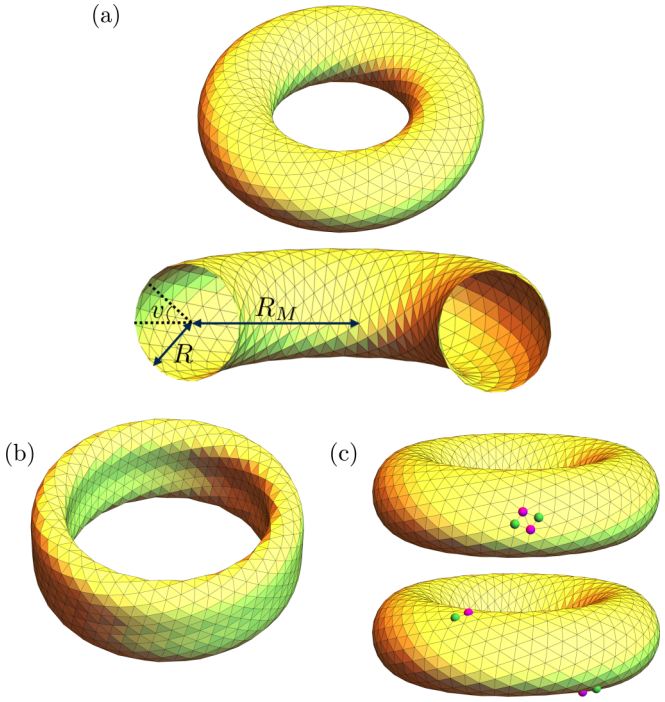

FIG. 12. (a),(b) Toroidal tubular crystal with $(m,n) = (14,18)$, with reduced bending rigidity $\tilde{\kappa} = 1$ (a) or 0.1 (b). Note the pinched sidewalls in (b). The bottom panel of (a) shows the torus major radius R_M, tubular crystal radius R, and the angular coordinate v. (c) Plastic deformation in the $(m,n) = (14,18)$ tubular crystal with $\tilde{\kappa} = 1$. (Top) A dislocation pair whose rightmost member has $\mathbf{b} = \mathbf{a}_1$ is nucleated near the outer equator. (Bottom) Under zero external stress, the dislocations spontaneously glide apart until coming to rest near the top and bottom of the torus.

crystal. Figure 12(b) shows that when the reduced bending rigidity $\tilde{\kappa} = \kappa/(Ya^2)$ is decreased from 1 to 0.1, the surface distorts into a pinched annulus structure with nearly flat sidewalls. The pinched structure is reminiscent of the instability of pressurized rings to deformations from circular to elliptical conformations [63]. To study dislocation nucleation and glide on a torus, we hereafter keep the bending rigidity fixed at $\tilde{\kappa} = 1$ to avoid this distortion.

The extensional strain u_{xx} present in the outer portion of the toroidal tubular crystal creates a stress σ_{xx} that should locally favor the appearance of tube-narrowing dislocation pairs. Indeed, we find numerically that even with zero externally imposed stress, a toroidal tubular crystal can be unstable to the nucleation and glide separation of dislocation pairs at its outer equatorial ring, where u_{xx} is greatest. This maximum strain u_{xx} is controlled by the aspect ratio of the tube, $\mathrm{AR} = R_M/R$, as the outer equatorial ring has circumference greater than the circumference R_M of the centerline by a factor $(1 + u_{xx})$ where $u_{xx} = R/R_M = 1/\mathrm{AR}$. In general, as a function of the angular coordinate v shown in Fig. 12(a), the axial strain is $u_{xx}(v) = (R/R_M)\cos v$.

The simplest application of what we have learned about cylindrical tubular crystals is to predict that dislocation pair nucleation and separation require a strain $u_{xx} \geqslant \sigma_c(\phi)/Y + \tilde{\kappa}(R_0/a)^{-2}$, where $\sigma_c(\phi)$ is the smallest critical stress $(\sigma_{xx} - \sigma_{yy})^{\dagger}_{\mathrm{eff}}$ at a given ϕ, as shown in Fig. 3(a) in units of $A = Y/(4\pi)$. Upon setting $u_{xx} = 1/\mathrm{AR}$, we obtain for the case of $(m,n) = (14,18)$ a prediction that the aspect ratio must be greater than ≈ 3.26 in order for dislocations to arise spontaneously. These dislocations will have $\mathbf{b} = \mathbf{a}_1$ for the right-moving dislocation, as is the case in Fig. 12(c). Numerically, we find that the critical aspect ratio lies between 2.9 and 3.3. On tori with larger aspect ratios (i.e., larger R_M, since fixing (m,n) fixes R) the dislocation pairs spontaneously annihilate as soon as they are created by a bond flip.

Attempts to create tube-narrowing dislocation pairs along the inside, top, or bottom regions of the torus resulted in immediate defect pair annihilation, as the torus there provides no stress to drive the dislocations apart. Along the inner portion of the torus, we expect that the compressional strain created by the torus geometry would result in formation and separation of tube-*widening* dislocation pairs. However, we did not observe such events in the simulated toroidal tubular crystals due to numerical instabilities. More realistic models of toroidal crystals would include unbound disclinations in the ground state to screen the local Gaussian curvature [64–66], which would interact in interesting and complex ways with gliding dislocations.

[1] I. Adler, D. Barabe, and R. V. Jean, Ann. Bot. (Oxford, UK) **80**, 231 (1997).
[2] C. Kuhlemeier, Trends Plant Sci. **12**, 143 (2007).
[3] R. V. Jean, *Phyllotaxis: A Systemic Study in Plant Morphogenesis* (Cambridge University Press, Cambridge, UK, 2009).
[4] M. F. Pennybacker, P. D. Shipman, and A. C. Newell, Phys. D (Amsterdam, Neth.) **306**, 48 (2015).
[5] L. S. Levitov, Phys. Rev. Lett. **66**, 224 (1991).
[6] L. S. Levitov, Europhys. Lett. **14**, 533 (1991).
[7] S. Douady and Y. Couder, Phys. Rev. Lett. **68**, 2098 (1992).
[8] C. Nisoli, N. M. Gabor, P. E. Lammert, J. D. Maynard, and V. H. Crespi, Phys. Rev. Lett. **102**, 186103 (2009).
[9] C. Nisoli, N. M. Gabor, P. E. Lammert, J. D. Maynard, and V. H. Crespi, Phys. Rev. E **81**, 046107 (2010).
[10] R. O. Erickson, Science **181**, 705 (1973).
[11] M. A. Lohr, A. M. Alsayed, B. G. Chen, Z. Zhang, R. D. Kamien, and A. G. Yodh, Phys. Rev. E **81**, 040401 (2010).
[12] A. Mughal, H. K. Chan, and D. Weaire, Phys. Rev. Lett. **106**, 115704 (2011).
[13] D. A. Wood, C. D. Santangelo, and A. D. Dinsmore, Soft Matter **9**, 10016 (2013).
[14] P. J. F. Harris, *Carbon Nanotube Science: Synthesis, Properties and Applications* (Cambridge University Press, Cambridge, UK, 2009).
[15] L. Bravais and A. Bravais, Ann. Sci. Nat. Bot. **7**, 42 (1837).
[16] W. F. Harris and R. O. Erickson, J. Theor. Biol. **83**, 215 (1980).

[17] A. Amir, J. Paulose, and D. R. Nelson, Phys. Rev. E **87**, 042314 (2013).
[18] G. Van Iterson, Ph.D. thesis, TU Delft, Delft University of Technology, 1907.
[19] A. Mughal and D. Weaire, Phys. Rev. E **89**, 042307 (2014).
[20] A. Mughal, H. K. Chan, D. Weaire, and S. Hutzler, Phys. Rev. E **85**, 051305 (2012).
[21] A. Mughal, Philos. Mag. **93**, 4070 (2013).
[22] B. I. Yakobson, Appl. Phys. Lett. **72**, 918 (1998).
[23] M. Buongiorno Nardelli, B. I. Yakobson, and J. Bernholc, Phys. Rev. Lett. **81**, 4656 (1998).
[24] M. Buongiorno Nardelli, B. I. Yakobson, and J. Bernholc, Phys. Rev. B **57**, R4277 (1998).
[25] B. I. Yakobson and P. Avouris, in *Carbon Nanotubes* (Springer, New York, 2001), pp. 287–327.
[26] D.-B. Zhang, R. James, and T. Dumitrică, J. Chem. Phys. **130**, 071101 (2009).
[27] H. F. Bettinger, T. Dumitrică, G. E. Scuseria, and B. I. Yakobson, Phys. Rev. B **65**, 041406 (2002).
[28] J. Y. Huang, S. Chen, Z. F. Ren, Z. Q. Wang, D. Z. Wang, M. Vaziri, Z. Suo, G. Chen, and M. S. Dresselhaus, Phys. Rev. Lett. **97**, 075501 (2006).
[29] D. Bozovic, M. Bockrath, J. H. Hafner, C. M. Lieber, H. Park, and M. Tinkham, Phys. Rev. B **67**, 033407 (2003).
[30] K. Suenaga, H. Wakabayashi, M. Koshino, Y. Sato, K. Urita, and S. Iijima, Nat. Nanotechnol. **2**, 358 (2007).
[31] M. Buongiorno Nardelli and J. Bernholc, Phys. Rev. B **60**, R16338 (1999).
[32] E. Nogales, Annu. Rev. Biochem. **69**, 277 (2000).
[33] V. Hunyadi, D. Chrétien, H. Flyvbjerg, and I. M. Jánosi, Biol. Cell **99**, 117 (2007).
[34] D. Chrétien, F. Metoz, F. Verde, E. Karsenti, and R. H. Wade, J. Cell Biol. **117**, 1031 (1992).
[35] D. R. Nelson, Annu. Rev. Biophys. **41**, 371 (2012).
[36] A. Amir and D. R. Nelson, Proc. Natl. Acad. Sci. USA **109**, 9833 (2012).
[37] D. R. Nelson and A. Amir, arXiv:1303.5896.
[38] A. Amir, F. Babaeipour, D. B. McIntosh, D. R. Nelson, and S. Jun, Proc. Natl. Acad. Sci. USA **111**, 5778 (2014).
[39] A. H. Church, *On the Relation of Phyllotaxis to Mechanical Laws* (Williams & Norgate, London, 1904).
[40] J.-F. Sadoc, N. Rivier, and J. Charvolin, Acta Crystallogr., Sect. A: Found. Crystallogr. **68**, 470 (2012).
[41] F. Rothen and A.-J. Koch, J. Phys.-Paris **50**, 633 (1989).
[42] D. R. Nelson, *Defects and Geometry in Condensed Matter Physics* (Cambridge University Press, Cambridge, UK, 2002).
[43] L. D. Landau and E. M. Lifshitz, *Elasticity theory* (Pergamon Press, Oxford, UK, 1975).
[44] J. P. Hirth and J. Lothe, *Theory of Dislocations* (Krieger, Malabar, FL, 1982).
[45] H. S. Seung and D. R. Nelson, Phys. Rev. A **38**, 1005 (1988).
[46] D. R. Nelson and B. I. Halperin, Phys. Rev. B **19**, 2457 (1979).
[47] R. Bruinsma, B. I. Halperin, and A. Zippelius, Phys. Rev. B **25**, 579 (1982).
[48] J. Lidmar, L. Mirny, and D. R. Nelson, Phys. Rev. E **68**, 051910 (2003).
[49] N. Yao and V. Lordi, J. Appl. Phys. **84**, 1939 (1998).
[50] J.-P. Salvetat, J.-M. Bonard, N. H. Thomson, A. J. Kulik, L. Forro, W. Benoit, and L. Zuppiroli, Appl. Phys. A: Mater. Sci. Process. **69**, 255 (1999).
[51] Q. Lu, M. Arroyo, and R. Huang, J. Phys. D: Appl. Phys. **42**, 102002 (2009).
[52] Y. Wei, B. Wang, J. Wu, R. Yang, and M. L. Dunn, Nano Lett. **13**, 26 (2012).
[53] A. Košmrlj and D. R. Nelson, Phys. Rev. B **93**, 125431 (2016)
[54] F. Ding, K. Jiao, M. Wu, and B. I. Yakobson, Phys. Rev. Lett. **98**, 075503 (2007).
[55] G. Gompper and D. M. Kroll, J. Phys. I **6**, 1305 (1996).
[56] http://www.alglib.net.
[57] D. Hilbert and S. Cohn-Vossen, *Geometry and the Imagination* (Chelsea Publishing, New York, 1952).
[58] J. Paulose, G. A. Vliegenthart, G. Gompper, and D. R. Nelson, Proc. Natl. Acad. Sci. USA **109**, 19551 (2012).
[59] L. Mahadevan, A. Vaziri, and M. Das, Europhys. Lett. **77**, 40003 (2007).
[60] V. Vitelli, J. B. Lucks, and D. R. Nelson, Proc. Natl. Acad. Sci. USA **103**, 12323 (2006).
[61] J. Liu, H. Dai, J. H. Hafner, D. T. Colbert, and R. E. Smalley, Nature (London) **385**, 780 (1997).
[62] R. Martel, H. R. Shea, and P. Avouris, Nature (London) **398**, 299 (1999).
[63] E. Katifori, Ph.D. thesis, Harvard University, 2008.
[64] L. Giomi and M. J. Bowick, Eur. Phys. J. E **27**, 275 (2008).
[65] L. Giomi and M. J. Bowick, Phys. Rev. E **78**, 010601 (2008).
[66] F. L. Jiménez, N. Stoop, R. Lagrange, J. Dunkel, and P. M. Reis, Phys. Rev. Lett. **116**, 104301 (2016).